network

MDPI

Article

Stochastic Dithered Phase Quantization for Beam-Space Enhancement in Multi-Bit Digital Coding Metasurfaces

Tanatorn Tantipiriyakul [1], Komsan Kanjanasit [2,*] and Panyayot Chaikan [1]

[1] Department of Computer Engineering, Faculty of Engineering, Prince of Songkla University, Songkhla 90110, Thailand; 6810130029@psu.ac.th (T.T.); panyayot.c@psu.ac.th (P.C.)
[2] College of Computing, Prince of Songkla University, Phuket Campus, Phuket 83120, Thailand
* Correspondence: komsan.k@psu.ac.th

Abstract

Digital coding metasurfaces (DCMs) manipulate electromagnetic waves through discrete phase control, but coarse phase quantization can generate coherent parasitic lobes and degrade beam-space performance. This paper proposes a stochastic dithered phase quantization (SDPQ) framework for 1–4-bit DCMs to improve radiation performance. Controlled random phase perturbations are introduced before quantization to redistribute spatially correlated quantization errors into diffuse scattering. The framework is evaluated through array-factor analysis and full-wave simulations of height-step reflectors, considering field fidelity, power-pattern similarity, parasitic- and quantization-lobe levels, steering accuracy, and beam efficiency. Compared with deterministic quantization, 2-bit SDPQ reduces the worst-case parasitic-lobe level from −7.4 to −10.6 dB and the maximum steering error from 1.9% to 0.8%. At unity dither strength, analytical quantization-lobe level reductions reach approximately 7.9 dB at both steering angles, while power-pattern similarity improves despite reduced complex-field fidelity. Full-wave sidelobe-level reductions reach 3.0–3.4 dB at 20° and 4.3–4.5 dB at 40°. The 1-bit DCM remains constrained by its inherent symmetric twin-beam response, whereas higher-bit DCMs offer greater phase accuracy but smaller additional sidelobe benefits. These findings identify four-state 2-bit SDPQ as a favorable low-resolution configuration, with dither strength balancing parasitic-lobe suppression, diffuse scattering, and beam preservation. The proposed framework offers a computationally scalable, hardware-agnostic phase-quantization strategy, subject to achievable phase and amplitude responses, for programmable metasurfaces and wireless beam steering.

Keywords: digital coding metasurfaces; stochastic dithering; phase quantization; beam-space performance; beam steering; reconfigurable intelligent surfaces (RIS); programmable metasurfaces

Check for updates

Academic Editor: Bin Han

Received: 13 August 2026
Revised: 27 October 2026
Accepted: 3 November 2026
Published: 4 November 2026

Copyright: © 2026 by the authors. Licensee MDPI, Basel, Switzerland. This article is an open access article distributed under the terms and conditions of the Creative Commons Attribution (CC BY) license.

1. Introduction

Digital coding metasurfaces (DCMs) synthesize electromagnetic wavefronts by assigning discrete reflection phases across an aperture [1–11]. Low-bit implementations are attractive because a small phase-state set can simplify unit cells and control networks, but coarse quantization can generate spatially correlated phase errors, coherent parasitic lobes, and beam-pointing errors [12–27]. Increasing the phase resolution reduces these errors at the expense of additional physical or control complexity. Existing mitigation approaches include discrete phase alignment, pre-phasing, optimized coding, and learning-assisted synthesis [28–40]. Their implementation requirements and objectives differ: pre-phasing

modifies the available spatial phase offsets, whereas optimization and learning select coding patterns through search or training. Dithered quantization offers a complementary mechanism. Random perturbations applied before quantization can reduce structured quantization artifacts, although their effects depend on the quantizer and dither distribution [41–49]. Related noise-shaping and dithering techniques have been applied to phased arrays, imaging, radar, and quantized communication systems [50–54].

1.1. Related Works

Phase quantization limits digital coding metasurfaces by approximating continuous phase profiles with discrete phase states. Low-bit DCMs, particularly 1-bit and 2-bit configurations, remain attractive for large-aperture programmable metasurfaces and RISs due to their relatively simple hardware and scalability.

1.1.1. Recent Advances in Quantization-Error Mitigation

To mitigate quantization-induced degradation, recent studies have explored phase optimization, AI-assisted coding synthesis, randomized coding, and optimization-based beam-forming [28,30,35–40]. These approaches improve coding synthesis, beam-forming performance, and electromagnetic field control. However, many rely on iterative optimization, data-driven training, or application-specific coding strategies, which can increase computational complexity for large-scale or real-time programmable metasurfaces. As summarized in Table 1, comparatively limited attention has been devoted to directly controlling the spatial structure of phase-quantization errors responsible for coherent sidelobes and quantization lobes in low-bit DCMs.

Table 1. Representative mitigation strategies for quantization and beam-forming degradation in programmable metasurfaces.

Ref.	Category	Key Contribution/Limitation
[28,30]	Phase optimization	Improves phase alignment and suppresses quantization lobes through fixed pre-phasing offsets combined with binary phase selection.
[35–37]	AI-based synthesis	Enables efficient coding synthesis and beam-forming, but does not explicitly target the spatial structure of phase-quantization errors.
[38]	Random coding	Controls statistical electromagnetic-field characteristics rather than directly addressing phase-quantization-induced beam-space artifacts.
[39,40]	Optimization-based beam-forming	Optimizes coding patterns for beam-forming and sidelobe control, but requires computational optimization.
This work	Stochastic dithered phase quantization	Low-bit SDPQ enhances sidelobe suppression and pattern similarity without adding physical phase states or fixed pre-phasing offsets.

1.1.2. Dithered Quantization and Error Engineering

Studies have shown that dithering can reduce the correlation between quantization errors and the input, redistributing structured distortion into noise-like spectra [42–46]. This approach has been applied to estimation, compressed sensing, imaging, beam-forming, radar, and wireless communications [47–54]. Representative dither-based techniques are summarized in Table 2. Previous studies have primarily employed dithering or noise shaping for array quantization-lobe suppression, image reconstruction, target recovery, or channel estimation. In contrast, the present work applies stochastic dithering directly to the phase quantization of multi-bit DCMs. The proposed SDPQ framework perturbs the continuous phase profile before discrete-state quantization to modify the spatial correlation and spectral distribution of quantization errors, with the objective of suppressing coherent beam-space artifacts without requiring iterative coding optimization.

Table 2. Representative dithering and noise-shaping techniques and their relation to the proposed SDPQ framework.

Ref.	Application	Key Difference from This Work
[50]	Phased arrays	FIR-based noise shaping for quantization-lobe suppression.
[51]	Sparse arrays	Extended noise shaping for lobe suppression and null restoration.
[52]	Fourier imaging	Evolutionary dithering for binary image reconstruction.
[53]	One-bit radar	Multiplicative phase dithering for sparse-target reconstruction.
[54]	One-bit MIMO	Gaussian dithering for channel estimation after ADC quantization.
This work	Multi-bit DCMs	Zero-mean stochastic phase perturbation before quantization for beam-space error redistribution and coherent-artifact suppression.

1.2. Research Gap and Contributions

Although widely used in signal processing, dithering remains insufficiently explored in digital coding metasurfaces, particularly its resolution-dependent effects on beam-space fidelity, sidelobes, quantization lobes, and steering accuracy. This work investigates stochastic dithered phase quantization across 1–4-bit metasurfaces using analytical beam synthesis and full-wave simulations of height-step DCM reflectors, without adding phase states.

The main contributions are:

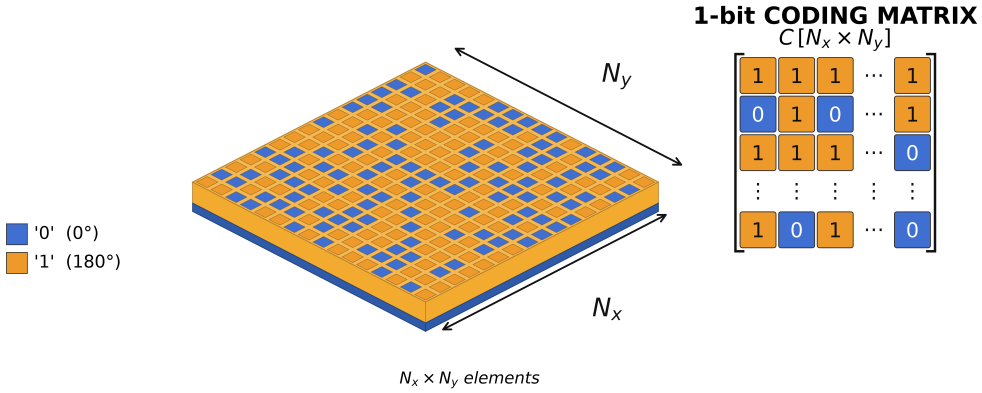
1. An SDPQ framework for 1–4-bit DCMs targeting coherent quantization artifacts.
2. A unified model combining phase generation, quantization, coding synthesis, and beam-space analysis.
3. Evaluation through array-factor analysis and full-wave simulations of height-step reflectors.
4. A comparative assessment of resolution-dependent beam-space performance and sidelobe trade-offs.

2. Materials and Methods

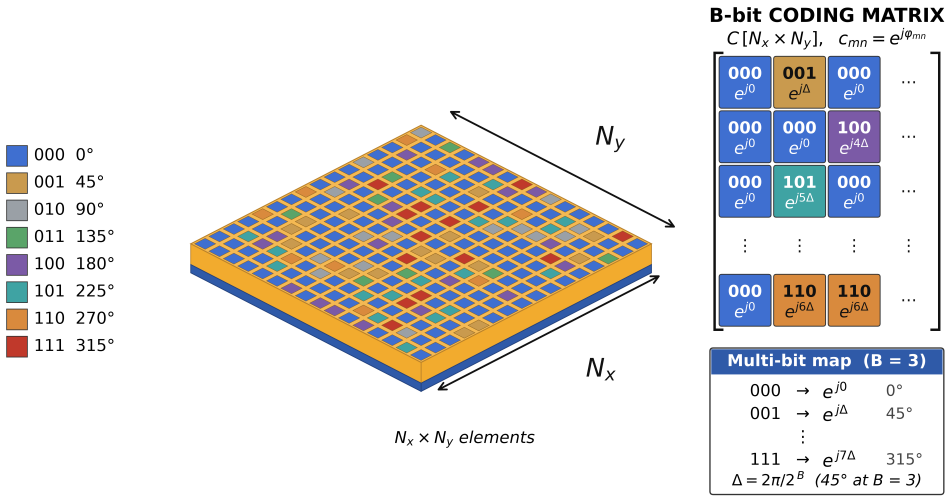
This section describes the SDPQ framework, including the metasurface model, dithering, quantization, and coding synthesis, followed by the height-step reflector and beam-space evaluation methodology.

2.1. Digital Coding Metasurface Model

A digital coding metasurface consists of a two-dimensional array of programmable unit cells, where each element is assigned a discrete coding state to manipulate the reflected electromagnetic wavefront. The spatial arrangement of these coding states is represented by a digital coding matrix, which establishes the relationship between the desired phase distribution and the physical implementation of the metasurface. Figure 1 illustrates the coding matrix representation for both 1-bit and generalized multi-bit digital coding metasurfaces.



(a) 1-bit coding metasurface



(b) B-bit coding metasurface

Figure 1. Coding matrix representations of digital coding metasurfaces (DCMs). (**a**) A 1-bit coding matrix with two discrete phase states (0 and 1), corresponding to reflection phases of 0° and 180°, respectively. (**b**) A generalized B-bit coding matrix, illustrated using a 3-bit DCM, where each unit cell is characterized by a quantized complex reflection coefficient $e^{j\phi_{m,n}}$.

For a 1-bit digital coding metasurface, each unit cell supports two discrete reflection phase states, denoted by the binary symbols '0' and '1', corresponding to reflection phases of approximately 0° and 180°, respectively. The resulting coding matrix is expressed as

$$\mathbf{C} = [c_{m,n}] \in \{0,1\}^{N_x \times N_y}, \tag{1}$$

where N_x and N_y denote the numbers of unit cells along the x- and y-directions, respectively, and $c_{m,n}$ is the binary coding state assigned to the (m,n)-th unit cell.

More generally, an b-bit digital coding metasurface provides $M = 2^b$ discrete reflection phase states, allowing finer control of the reflected wavefront. The coding matrix is therefore represented as

$$\mathbf{C} = \left[e^{j\phi_{m,n}}\right], \qquad \phi_{m,n} \in \left\{0, \frac{2\pi}{M}, \frac{2(2\pi)}{M}, \ldots, \frac{(M-1)2\pi}{M}\right\}, \tag{2}$$

where $\phi_{m,n}$ denotes the quantized reflection phase assigned to the (m, n)-th unit cell. Increasing the phase resolution increases the number of available coding states, enabling a more accurate approximation of the desired continuous phase distribution and consequently improving wavefront reconstruction and beam-forming performance.

The coding matrix defines the spatial phase distribution across the metasurface aperture for beam synthesis. An ideal continuous phase profile is first calculated for the desired steering direction and then quantized into discrete coding states according to the available phase resolution. The resulting coding matrix is subsequently mapped to the unit-cell configuration for analytical and full-wave beam synthesis. The quantization procedure is described in the following subsection.

2.2. Phase Synthesis and Stochastic Quantization

2.2.1. Uniform Dither Signal Model

To decorrelate the spatial distribution of phase quantization errors, a uniform dither signal is introduced before phase discretization. The dither signal applied to each metasurface element is modeled as

$$d(m, n) \sim U\left(-\frac{\alpha\Delta}{2}, +\frac{\alpha\Delta}{2}\right), \tag{3}$$

where $U(\cdot)$ denotes the uniform distribution, $\Delta = 2\pi/2^B$ is the phase quantization interval for a B-bit metasurface, and α is the dither strength controlling the perturbation amplitude. The dither strength $\alpha \geq 0$ is evaluated. Here, $\alpha = 0$ provides deterministic quantization, while $\alpha = 1$ yields a dither range of $[-\Delta/2, \Delta/2]$, spanning one quantization interval. Values $\alpha > 1$ introduce stronger perturbations.

The uniform dither signal has a zero-mean distribution and bounded amplitude, ensuring that no systematic phase bias is introduced during quantization while maintaining low computational complexity. By randomly perturbing phase values near quantization boundaries, the proposed approach reduces the spatial correlation of quantization errors without altering the overall phase gradient. Consequently, coherent quantization artifacts are expected to be redistributed into diffuse noise-like components, providing a theoretical basis for improving beam synthesis performance.

2.2.2. Ideal Continuous Phase Distribution

Programmable digital coding metasurfaces manipulate electromagnetic wavefronts by imposing a spatially varying reflection phase across the metasurface aperture. To steer the reflected beam toward a desired direction, the reflection phase of each unit cell is designed to satisfy a prescribed linear phase gradient derived from the generalized Snell's law. This continuous phase distribution represents the ideal phase profile before digital phase quantization is applied.

Consider a planar digital coding metasurface consisting of $N_x \times N_y$ programmable unit cells with a uniform element spacing p. The coordinates of the (m, n)-th unit cell are defined as

$$x_m = mp, \qquad y_n = np, \tag{4}$$

where $m = 0, 1, \ldots, N_x - 1$ and $n = 0, 1, \ldots, N_y - 1$.

For a desired beam-steering direction specified by elevation angle θ_0 and azimuth angle ϕ_0, the corresponding direction cosines are

$$u_0 = \sin\theta_0 \cos\phi_0, \qquad v_0 = \sin\theta_0 \sin\phi_0. \tag{5}$$

The ideal continuous reflection phase required at each metasurface element is then yielded by

$$\phi_{\text{ideal}}(m, n) = -k_0(x_m u_0 + y_n v_0), \tag{6}$$

where

$$k_0 = \frac{2\pi}{\lambda} \tag{7}$$

is the free-space wavenumber, and λ denotes the operating wavelength.

Since the reflection phase is periodic over 2π, the implemented phase profile is wrapped into the interval $[0, 2\pi)$ as

$$\phi_{\text{ideal}}(m, n) = \text{mod}[-k_0(x_m u_0 + y_n v_0), 2\pi]. \tag{8}$$

Equation (8) defines a continuous linear phase gradient across the metasurface aperture. The slope of the phase gradient determines the steering angle of the reflected beam, while the phase variation becomes increasingly rapid as the desired steering angle increases. Consequently, large-angle beam steering requires steeper phase gradients and imposes more stringent requirements on the phase resolution of the digital coding metasurface.

For an ideal continuously tunable metasurface, the phase profile in Equation (8) can be implemented exactly, producing the desired reflected beam without phase-quantization artifacts. In practice, however, programmable metasurfaces can realize only a finite number of discrete phase states determined by the digital coding resolution. Therefore, the continuous phase distribution must be approximated through digital phase quantization, introducing unavoidable phase quantization errors that degrade the far-field radiation characteristics.

2.2.3. Deterministic Phase Quantization

The reflection phase required for beam steering is continuous, whereas practical digital coding metasurfaces can realize only a finite number of discrete phase states determined by the coding resolution. Consequently, the ideal phase profile must be quantized before implementation.

For a desired beam direction (θ_0, ϕ_0), the ideal reflection phase is first described by Equation (8). For a uniformly spaced metasurface with normalized element coordinates $x_m = mp$ and $y_n = np$, the discrete phase profile becomes

$$\phi_{\text{ideal}}(m, n) = \text{mod}[-2\pi p(mu_0 + nv_0), 2\pi], \tag{9}$$

where u_0 and v_0 denote the normalized directional cosines defined in Equation (5).

For a B-bit digital coding metasurface, the number of available phase states is $N_s = 2^B$, and the corresponding phase quantization interval is $\Delta = 2\pi/2^B$. Each element is assigned to its nearest phase state,

$$s(m, n) = \text{round}\left(\frac{\phi_{\text{ideal}}(m, n)}{\Delta}\right) \bmod 2^B, \tag{10}$$

yielding the implemented phase

$$\phi_q(m,n) = s(m,n)\Delta \tag{11}$$

and the phase error

$$\varepsilon(m,n) = \phi_q(m,n) - \phi_{\text{ideal}}(m,n), \tag{12}$$

bounded by

$$-\frac{\Delta}{2} \le \varepsilon(m,n) < \frac{\Delta}{2}. \tag{13}$$

Although deterministic quantization minimizes the phase error of each element, the resulting errors are spatially correlated, producing coherent quantization lobes and elevated sidelobes, particularly for low-bit coding metasurfaces. Increasing the phase resolution reduces the quantization interval and improves beam-space performance, but residual periodic errors remain even at higher resolutions.

2.2.4. Stochastic Dithered Phase Quantization

To decorrelate the periodic phase errors produced by deterministic quantization, the proposed framework introduces a uniformly distributed random perturbation prior to phase discretization. For a B-bit coding metasurface, the coding state is provided by

$$s(m,n) = \text{mod}\left(\left\lfloor \frac{\phi_{\text{ideal}}(m,n) + d(m,n)}{\Delta} + \frac{1}{2} \right\rfloor, 2^B\right), \tag{14}$$

where $d(m,n)$ denotes an independent and identically distributed (i.i.d.) zero-mean uniform phase perturbation. From Equation (3), its mean and variance are shown by

$$\mathbb{E}[d(m,n)] = 0, \qquad \text{Var}[d(m,n)] = \frac{\alpha^2\Delta^2}{12}. \tag{15}$$

Dissimilar deterministic phase quantization and stochastic dithering introduce independent random perturbations that reduce spatial correlations in quantization errors while approximately preserving the desired phase distribution. Consequently, coherent quantization artifacts are redistributed into a more diffuse spectral background, suppressing parasitic lobes while generally maintaining beam-steering accuracy. This behavior is consistent with nonsubtractive dithered quantization theory, although complete spectral whitening is not guaranteed and depends on phase resolution and dither strength. The improvement is most pronounced for low-bit coding metasurfaces, whereas higher phase resolutions exhibit diminishing benefits because their deterministic phase profiles more closely approximate the ideal distribution. Thus, SDPQ provides a practical trade-off between parasitic-lobe suppression, diffuse scattering, and main-beam efficiency.

Algorithm 1 summarizes the generation of deterministic and stochastic dithered coding matrices. For each metasurface element, the ideal wrapped phase is computed and either directly quantized or quantized after adding a uniformly distributed random variable ($d(m,n)$). The resulting coding-state and quantized phase matrices are then used for beam synthesis. Both methods require $\mathcal{O}(N_x N_y)$ computational complexity, with stochastic quantization adding only one random number generation per element.

The aperture phase-error analysis is presented in Appendix A, where deterministic phase quantization (DQ) and stochastic dithered phase quantization (SDPQ) are compared against the ideal continuous phase distribution. Element-wise phase errors and their spatial distributions are examined to illustrate the effects of stochastic dithering on aperture quantization errors.

Algorithm 1 General Digital Coding Matrix Generation

Require: Steering direction (θ_0, ϕ_0), bit resolution B, array dimensions N_x and N_y, element spacing p, wavelength λ, dither strength α, and Mode $\in$ {Deterministic, Dithered}
Ensure: Coding-state matrix $\mathbf{S}$ and quantized phase matrix $\mathbf{\Phi}_q$

$N_{\text{state}} \leftarrow 2^B$
$\Delta \leftarrow 2\pi / N_{\text{state}}$
$u_0 \leftarrow \sin(\theta_0)\cos(\phi_0)$
$v_0 \leftarrow \sin(\theta_0)\sin(\phi_0)$
for $m = 0$ to $N_x - 1$ **do**
  for $n = 0$ to $N_y - 1$ **do**
    $\phi_{\text{ideal}}(m,n) \leftarrow \text{mod}\left(-\frac{2\pi p}{\lambda}(mu_0 + nv_0),\, 2\pi\right)$
    if Mode = Deterministic **then**
      $\widetilde{\phi}(m,n) \leftarrow \phi_{\text{ideal}}(m,n)$
    else
      Generate $d(m,n) \sim \mathcal{U}\left(-\frac{\alpha\Delta}{2}, +\frac{\alpha\Delta}{2}\right)$
      $\widetilde{\phi}(m,n) \leftarrow \text{mod}(\phi_{\text{ideal}}(m,n) + d(m,n),\, 2\pi)$
    end if
    $s(m,n) \leftarrow \text{mod}\left(\text{round}\left(\frac{\widetilde{\phi}(m,n)}{\Delta}\right), N_{\text{state}}\right)$
    $\mathbf{S}(m,n) \leftarrow s(m,n)$
    $\mathbf{\Phi}_q(m,n) \leftarrow s(m,n)\Delta$
  end for
end for

return $\mathbf{S}, \mathbf{\Phi}_q$

2.3. Physical Height-Step DCM Configurations

To physically realize the quantized reflection phases required by the proposed phase-dithered digital coding metasurface, a metallic height-step unit cell is employed. The proposed design controls the reflection phase by varying the physical height of each perfect electric conductor (PEC) unit cell while maintaining an approximately constant reflection magnitude. This passive phase-control mechanism provides a simple, low-complexity, and efficient implementation for generating discrete phase states required for beam steering.

Figure 2 illustrates the operating principle of the height-step reflection-phase design. As shown in Figure 2a, increasing the cell height by h shortens the round-trip propagation path of the reflected wave by $2h$, producing a reflection-phase advance provided by

$$\Delta\phi = 2kh = \frac{4\pi h}{\lambda}, \tag{16}$$

where $k = 2\pi/\lambda$ is the free-space wavenumber and λ is the operating wavelength. Consequently, the reflection phase varies linearly with the cell height, enabling a direct mapping between the desired phase state and the corresponding physical geometry.

Figure 2b presents the phase-to-height mapping for a 4-bit digital coding metasurface operating at 10 GHz. Sixteen discrete phase states spanning 0° to 337.5° are uniformly quantized with a phase resolution of 22.5°. According to the linear relationship between phase and height, the corresponding height increment is

$$\Delta h = \frac{\lambda}{32}, \tag{17}$$

resulting in sixteen equally spaced height levels that realize the complete 4-bit phase library.

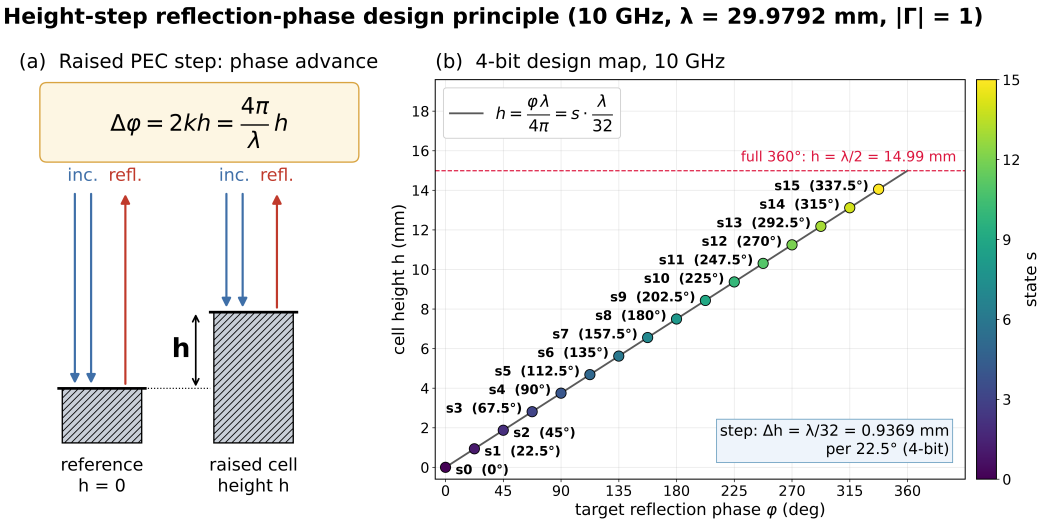


Figure 2. Height-step reflection-phase design principle for the proposed digital coding metasurface operating at 10 GHz. (**a**) Reflection-phase variation produced by changing the PEC unit-cell height. (**b**) Phase-to-height mapping for the 16 quantized phase states of a 4-bit digital coding metasurface, where each state corresponds to a height increment of $\lambda/32$.

Figure 3 shows the theoretical reflection-phase response of the proposed 4-bit height-step PEC unit cell. At 10 GHz, its 16 uniformly spaced states provide a 22.5° phase resolution. The phase variation over 8–12 GHz reflects the true-time-delay behavior associated with the height differences.

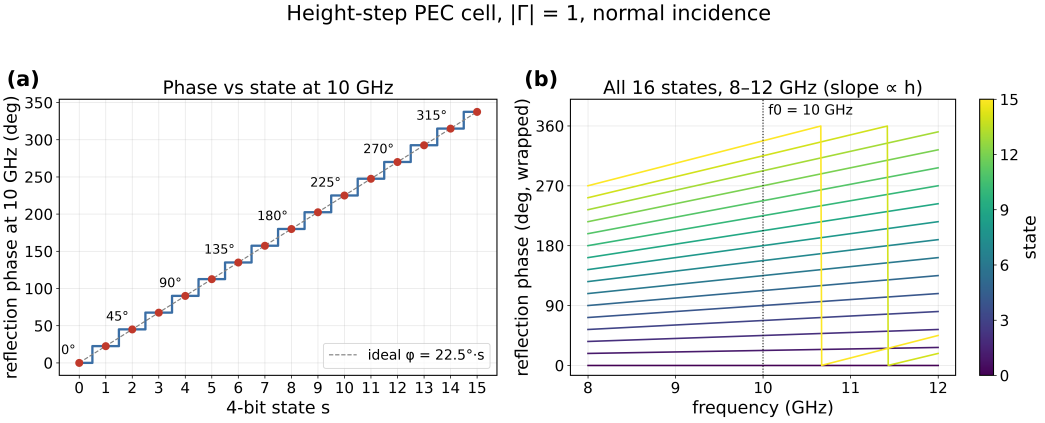


Figure 3. Theoretical reflection-phase response of the proposed 4-bit height-step PEC unit cell. (**a**) Quantized reflection phase at 10 GHz with 16 uniformly spaced phase states. (**b**) Reflection-phase responses of all states over 8–12 GHz, illustrating the true-time-delay characteristic for multi-bit phase control.

2.4. Beam-Space Performance Evaluation

To evaluate the proposed stochastic dithered phase quantization framework, the generated coding matrices are converted into discrete reflection-phase distributions according to the selected phase resolution. The analytical model considers a uniform planar array of isotropic elements with unit reflection amplitude, $|\Gamma| = 1$, while mutual coupling and element-pattern effects are neglected. The far-field response is synthesized using the array factor (AF), providing a computationally efficient framework for comparing DQ and SDPQ.

For an $N_x \times N_y$ DCM, the array factor is expressed as

$$AF(\theta, \varphi) = \sum_{m=0}^{N_x-1} \sum_{n=0}^{N_y-1} \exp\{j[\phi_q(m,n) + k_0 p(mu + nv)]\}, \tag{18}$$

where $\phi_q(m,n)$ denotes the quantized reflection phase assigned to the (m,n)-th metasurface element, p is the element spacing, and k_0 is the free-space wavenumber (Equation (7)). The variables u and v denote the direction cosines (Equation (5)) corresponding to the elevation angle θ and azimuth angle φ, respectively. The symbol φ is used for the azimuth angle to distinguish it from the quantized reflection phase $\phi_q(m,n)$.

The normalized radiation power pattern is calculated as

$$P(u,v) = \frac{|AF(u,v)|^2}{\max\limits_{u,v} |AF(u,v)|^2}, \tag{19}$$

and its logarithmic representation is

$$P_{\mathrm{dB}}(u,v) = 10 \log_{10}[P(u,v)]. \tag{20}$$

The synthesized patterns are evaluated over the visible region, $u^2 + v^2 \leq 1$, together with E-plane cuts at $\varphi = 0^\circ$. The analytical investigation considers 1-, 2-, 3-, and 4-bit DCMs with E-plane steering from -50° to $+50^\circ$, with the 20° and 40° cases examined in greater detail. For SDPQ, independent stochastic realizations are generated for each configuration, and ensemble statistics are used to characterize the resulting beam-space performance.

To provide a comprehensive comparison, several complementary metrics are employed. Because stochastic dithering can modify the complex field while preserving the overall radiation-pattern shape, complex-field fidelity and power-pattern similarity are evaluated separately.

The complex-field fidelity is defined as

$$F_{\mathrm{field}} = \frac{|\langle A_{\mathrm{ideal}}, A_{\mathrm{actual}} \rangle|^2}{\|A_{\mathrm{ideal}}\|^2 \|A_{\mathrm{actual}}\|^2}, \tag{21}$$

where A_{ideal} and A_{actual} denote the complex far-field distributions of the continuous-phase reference and the quantized DCM, respectively. This metric accounts for both amplitude and phase agreement and satisfies $0 \leq F_{\mathrm{field}} \leq 1$.

To separately quantify similarity between the normalized radiation-power patterns, the pattern-similarity metric is defined as

$$S_P = \frac{\langle P_{\mathrm{ideal}}, P_{\mathrm{actual}} \rangle}{\|P_{\mathrm{ideal}}\| \|P_{\mathrm{actual}}\|}, \tag{22}$$

where P_{ideal} and P_{actual} are the corresponding power distributions over the evaluated beam space. A value approaching unity indicates strong agreement in radiation-pattern shape.

The sidelobe level (SLL) is defined relative to the main-beam peak as

$$\mathrm{SLL} = 10 \log_{10}\left(\frac{P_{\mathrm{side,max}}}{P_{\mathrm{main}}}\right), \tag{23}$$

where $P_{\mathrm{side,max}}$ is the strongest visible sidelobe outside the main-beam region, and P_{main} is the main-beam peak power. For the 1-bit case, the inherent symmetric twin beam is excluded from the sidelobe search.

The quantization-lobe level (QLL) is additionally employed to characterize coherent parasitic radiation associated specifically with phase quantization. It is evaluated relative to the main-beam peak as

$$\mathrm{QLL} = 10\log_{10}\left(\frac{P_{\mathrm{QL,max}}}{P_{\mathrm{main}}}\right), \tag{24}$$

where $P_{\mathrm{QL,max}}$ denotes the peak power of the identified quantization-lobe component outside the main-beam region. More negative QLL values therefore indicate stronger suppression of coherent quantization artifacts.

Beam-steering accuracy is quantified by

$$\Delta\theta = \left|\theta_{\mathrm{target}} - \theta_{\mathrm{peak}}\right|, \tag{25}$$

where θ_{target} is the prescribed steering angle, and θ_{peak} is the direction of the synthesized main-beam maximum. Where appropriate, the steering error is also reported as a percentage relative to the target steering angle.

Beam efficiency is evaluated as the fraction of radiated power contained within the prescribed main-beam region,

$$\eta_{\mathrm{beam}} = \frac{\iint_{\Omega_{\mathrm{MB}}} P(u,v)\,du\,dv}{\iint_{\Omega_{\mathrm{vis}}} P(u,v)\,du\,dv}, \tag{26}$$

where Ω_{MB} denotes the main-beam region and Ω_{vis} represents the complete visible region. The mean radiation floor outside the excluded main-beam region is also monitored to quantify the extent to which stochastic dithering redistributes coherent quantization artifacts into diffuse background radiation.

Main-beam loss (MBL) quantifies the reduction in radiation intensity at the desired steering direction relative to the ideal continuous-phase reference and is defined as

$$\mathrm{MBL} = 10\log_{10}\left(\frac{|AF_{\mathrm{ideal}}(u_0,v_0)|^2}{|AF_q(u_0,v_0)|^2}\right) \quad \mathrm{dB}, \tag{27}$$

where AF_{ideal} and AF_q denote the ideal and quantized array factors, respectively. A lower MBL indicates better main-beam preservation, with 0 dB corresponding to the ideal continuous-phase reference.

The mean diffuse floor (MDF) measures the average normalized radiation power outside the main-beam region, defined as

$$\mathrm{MDF} = 10\log_{10}\left[\frac{1}{|\Omega_{\mathrm{ex}}|}\iint_{\Omega_{\mathrm{ex}}}\frac{|AF_q(u,v)|^2}{P_{\mathrm{ref}}}\,du\,dv\right] \quad \mathrm{dB}, \tag{28}$$

where Ω_{ex} is the visible region excluding the main beam, and P_{ref} is the fixed reference power. A lower MDF indicates weaker diffuse scattering.

2.5. Analytical Array-Factor Configuration and Monte Carlo Evaluation

The analytical array-factor and statistical evaluation configuration used throughout this study is summarized in Table 3. A 16×16 DCM operating at $f_0 = 10$ GHz is considered, with an inter-element spacing of $p = \lambda_0/2$. Each element is modeled as an isotropic reflector with unit-magnitude reflection amplitude; mutual coupling and the individual element factor are neglected in the analytical formulation. Phase resolutions from 1 to 4 bits are investigated, with E-plane steering evaluated over $\theta_0 = \pm 10^\circ$ to $\pm 50^\circ$. DQ corresponds to $\alpha = 0$, whereas SDPQ employs a zero-mean uniform phase dither. The dither strength

is varied from $\alpha = 0$ to 2, with $\alpha = 1$ adopted as the reference condition for the detailed SDPQ analysis.

Because SDPQ is stochastic, its performance is evaluated using a Monte Carlo procedure rather than a single random realization. For each SDPQ configuration, $R = 96$ independent realizations are generated using $\text{seed}_k = 1000B + \theta_0 + k$, where B denotes the phase resolution in bits, θ_0 is the target beam-steering angle in degrees, and $k = 1, \ldots, 96$ is the realization index. All beam-space metrics are calculated independently for each realization and subsequently reported as ensemble means ($\bar{X}$) with two-sided 95% confidence intervals ($\text{CI}_{95\%}$),

$$\bar{X} = \frac{1}{R} \sum_{k=1}^{R} X_k, \tag{29}$$

$$\text{CI}_{95\%} = \bar{X} \pm t_{0.975,R-1} \frac{s_X}{\sqrt{R}}, \tag{30}$$

where X_k denotes the metric obtained from the kth realization, s_X is the sample standard deviation, and $t_{0.975,95} = 1.985$ for $R = 96$. This Monte Carlo procedure quantifies realization-to-realization variability and ensures that the reported SDPQ performance reflects statistically averaged behavior rather than a particular random coding matrix. The far field is sampled on a 401×401 (u, v) grid. The evaluated metrics include F_{field}, S_P, SLL, QLL, beam efficiency, mean radiation floor, and steering error.

Table 3. Setup of the analytical array-factor model.

Parameter	Analytical Model (Array Factor)
Frequency	f_0 = 10 GHz (λ_0 = 29.979 mm)
Array	16 × 16 cells, spacing p = $\lambda_0/2$ = 14.99 mm
Element model	Isotropic, unit amplitude ($\|\Gamma\| = 1$); phase s·Δ; no coupling, no element factor
Phase resolution	B = 1–4 bit, $\Delta = 2\pi/2^B$ (180°, 90°, 45°, 22.5°)
Steering	E-plane ($\phi_0 = 0°$), $\theta_0 = \pm 10°$ to $\pm 50°$; 20° and 40° in detail
Quantizers	DQ ($\alpha = 0$); SDPQ, dither $U(-\alpha\Delta/2, \alpha\Delta/2)$, α = 0–2 ($\alpha = 1$ default)
Realizations	R = 96 per SDPQ case (seeds 1000·B + θ_0 + k); mean and 95 % CI (t = 1.985)
Far-field grid	401 × 401 points, u, v ∈ [−1, 1]; visible region $u^2 + v^2 \leq 1$
Power scale	$P = \|AF\|^2/N^4$ (0 dB = uniform broadside beam)
Metrics	F_{field}, S_P, SLL, QLL, beam efficiency, mean floor, steering error

In practical implementations, amplitude non-uniformity, phase-dependent losses, and mutual coupling may reduce main-beam efficiency, alter sidelobe characteristics, and affect the spatial error-redistribution mechanism of SDPQ. Consequently, parasitic-lobe suppression and beam-space fidelity may differ from idealized predictions. Although SDPQ is hardware-agnostic in principle, its performance has not been experimentally demonstrated to be hardware-independent. The present Monte Carlo evaluation captures stochastic phase-quantization variations but excludes hardware-dependent effects, which require further full-wave and experimental validation.

3. Results and Discussion

This section presents the performance evaluation of the proposed SDPQ framework for multi-bit DCMs. Deterministic and stochastic dithered quantization are compared for 1-, 2-, 3-, and 4-bit phase resolutions to evaluate beam synthesis performance.

3.1. Beam-Space Responses Across Phase Resolutions

This subsection compares DQ and SDPQ across 1–4-bit DCMs through far-field patterns, beam-steering performance, field fidelity, and power-pattern similarity.

3.1.1. Comparative Beam-Steering Far-Field Analysis

The comparison of the beam-space responses of the 1-bit to 4-bit DCM with DQ and SDPQ is illustrated for steering angles from $\pm 10^\circ$ to $\pm 50^\circ$. Figure 4 presents four representative beam-space responses of the 1-bit DCM at steering angles from $+10^\circ$ to $+40^\circ$, within the investigated range of $\theta_0 = \pm 10^\circ, \pm 20^\circ, \pm 30^\circ, \pm 40^\circ, \pm 50^\circ$. Deterministic quantization produces structured binary coding and pronounced quantization lobes, with steering errors of 0.5–3.7%. Stochastic dithering redistributes coherent quantization artifacts into a diffuse background while largely preserving the desired beam direction. Steering errors are $\leq$1.6% except at 10°, where the error reaches 5.0%. The worst parasitic-lobe levels remain comparable, ranging from -11.3 to -6.6 dB with dithering. Meanwhile, the average radiation floor rises from a range of -27.6 to -23.6 dB to -20.4 to -17.1 dB, consistent with increased diffuse scattering rather than systematic suppression of the strongest parasitic lobe.

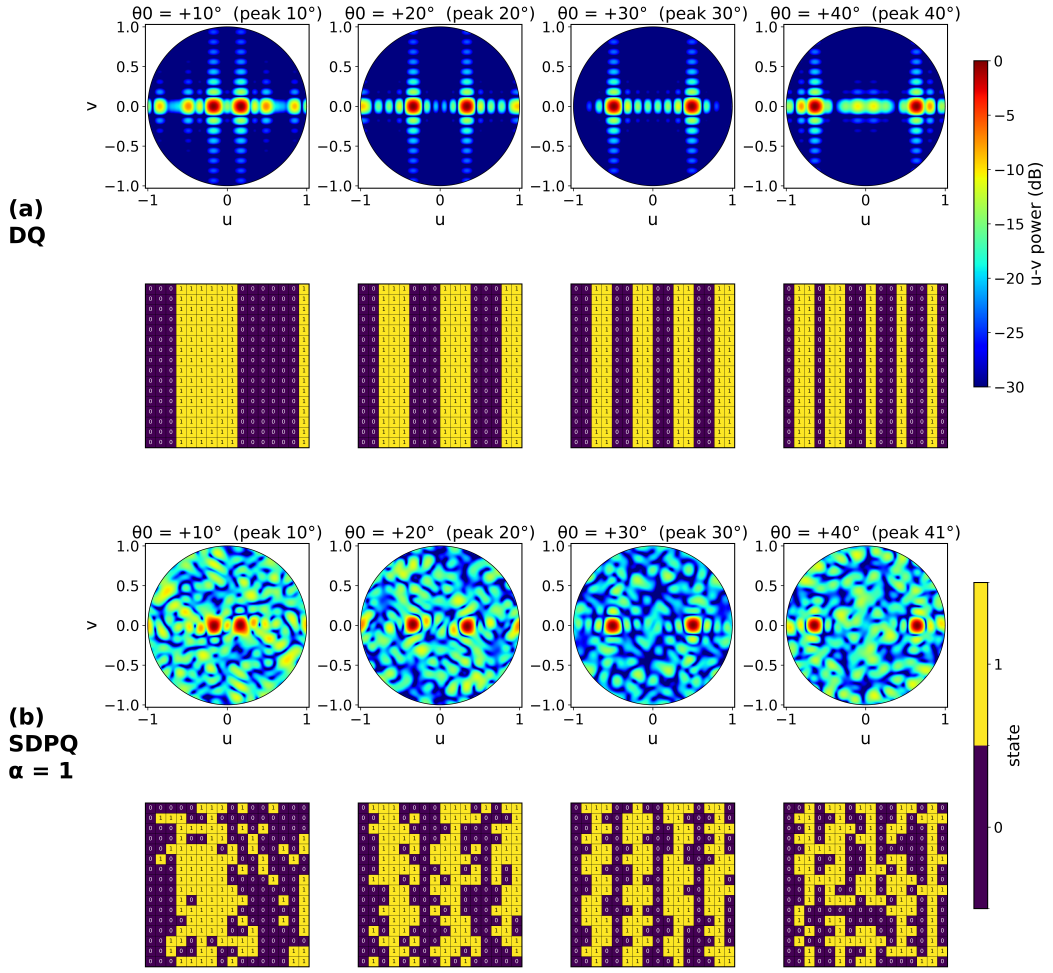


Figure 4. Representative comparison of (**a**) DQ (deterministic) and (**b**) SDPQ (stochastic dithered) beam-space responses and corresponding coding matrices of a 1-bit digital coding metasurface for E-plane beam steering over scanning angles from $+10^\circ$ to $+40^\circ$.

Figure 5 shows four representative beam-space responses of the 2-bit DCM corresponding to steering angles of +10°, +20°, +30°, and +40°. The comprehensive analysis is conducted over the steering range of ±10° to ±50°. Compared with the 1-bit DCM, the finer four-level phase quantization reduces coherent quantization lobes, achieving steering errors of 0–1.9%, worst parasitic lobes of −7.4 to −13.1 dB, and an average radiation floor of −26.9 to −30.5 dB. Stochastic dithering further suppresses residual coherent sidelobes while preserving beam-pointing accuracy, reducing the worst parasitic lobe by approximately 3 dB to −10.6 to −13.1 dB. The average radiation floor increases slightly to −25.0 to −30.5 dB due to energy redistribution into a diffuse background.

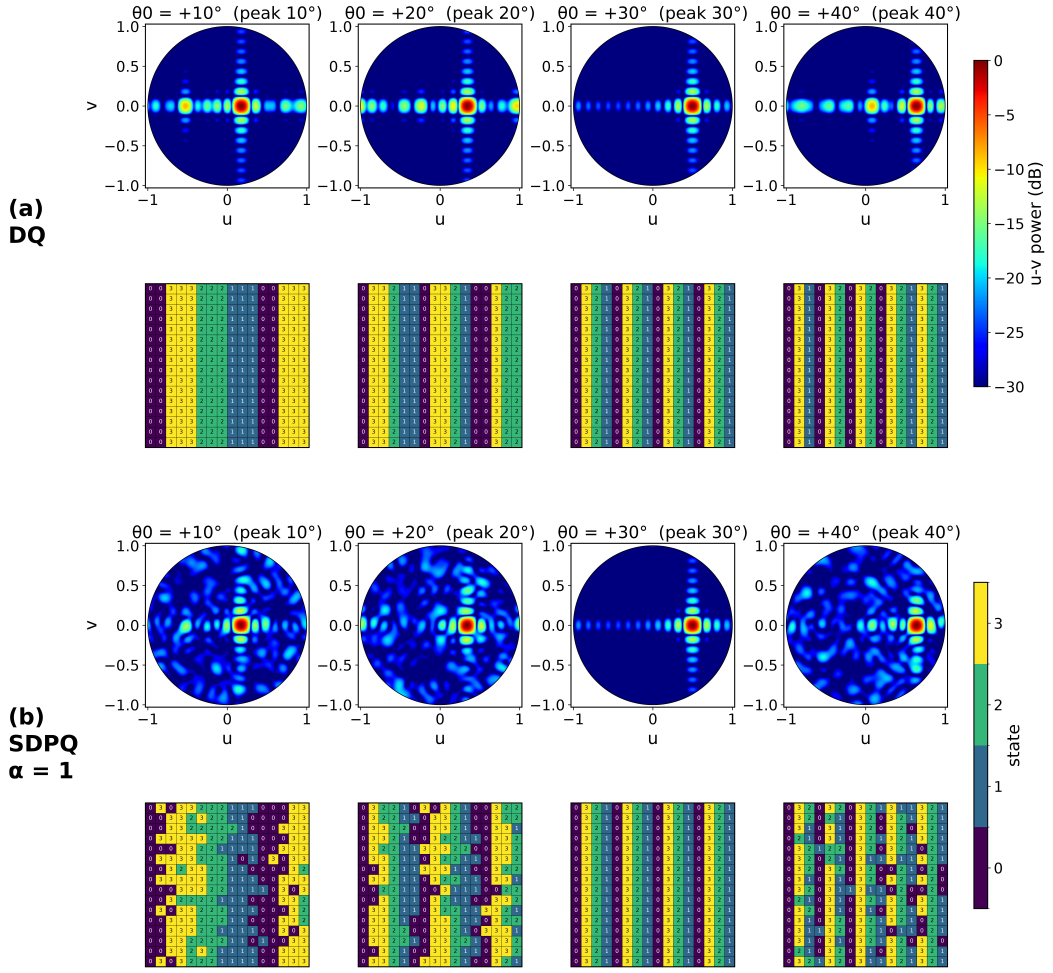


Figure 5. Representative comparison of (**a**) DQ (deterministic) and (**b**) SDPQ (stochastic dithered) beam-space responses and corresponding coding matrices of a 2-bit DCM for E-plane beam steering over scanning angles from +10° to +40°.

Figure 6 shows four representative beam-space responses of the 3-bit DCM corresponding to steering angles of +10°, +20°, +30°, and +40°. The analysis is performed over the steering range of ±10° to ±50°. Owing to the finer 45° phase resolution, deterministic quantization already achieves excellent beam steering with errors of 0–1.6%, worst parasitic lobes of −9.3 to −13.1 dB, and an average radiation floor of −29.3 to −30.5 dB. Stochastic dithering further randomizes the residual phase errors while preserving beam-pointing accuracy, reducing the worst parasitic lobes to −12.0 to −13.1 dB, whereas the average radiation floor changes only slightly to −28.7 to −30.5 dB.

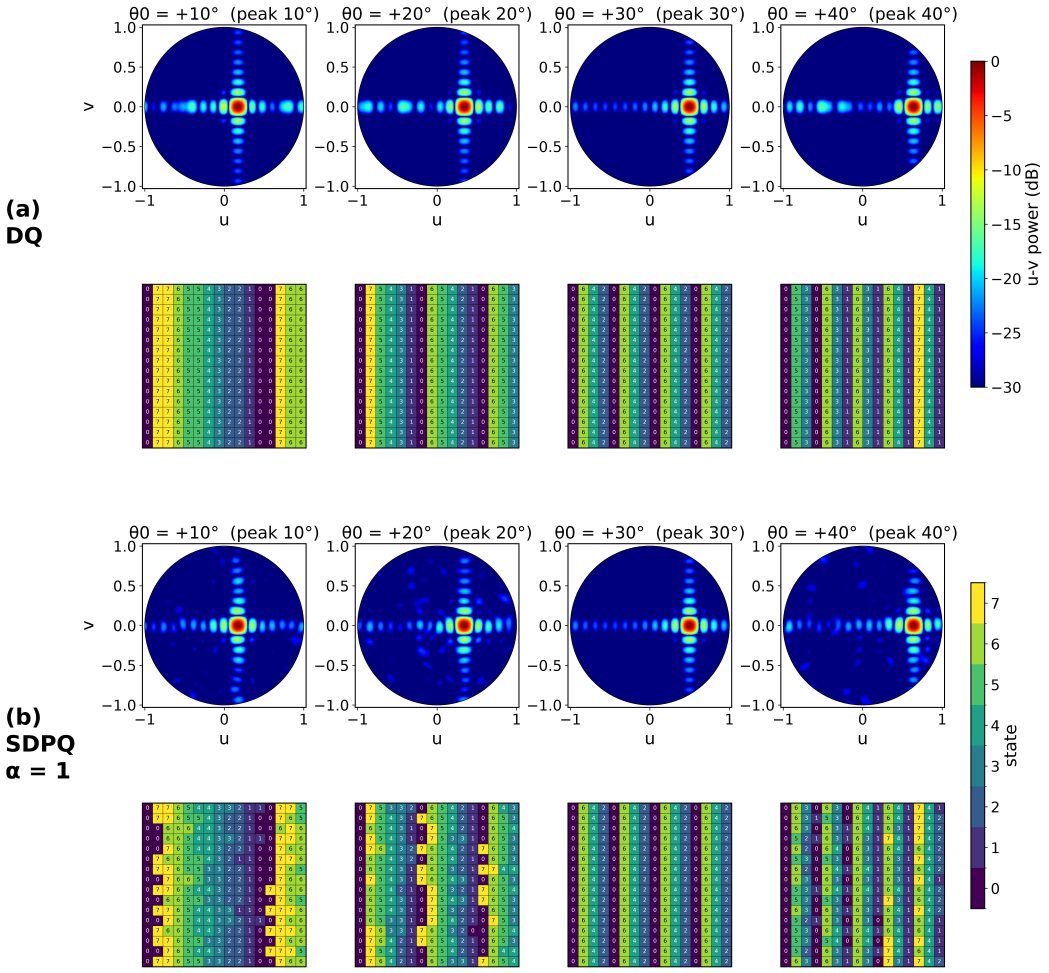


Figure 6. Representative comparison of (**a**) DQ (deterministic) and (**b**) SDPQ (stochastic dithered) beam-space responses and corresponding coding matrices of a 3-bit DCM for E-plane beam steering over scanning angles from $+10^\circ$ to $+40^\circ$.

Figure 7 illustrates four representative beam-space responses of the 4-bit DCM at steering angles of $+10^\circ$, $+20^\circ$, $+30^\circ$, and $+40^\circ$. The complete analysis is conducted over steering angles from $\pm 10^\circ$ to $\pm 50^\circ$. Owing to the fine 22.5° phase resolution, deterministic quantization already achieves near-ideal beam steering with errors of only 0–0.9%, worst parasitic lobes of -11.8 to -13.1 dB, and an average radiation floor of -30.1 to -30.5 dB. Stochastic dithering produces nearly identical beam characteristics, maintaining steering errors below 0.8%, worst parasitic lobes of -12.7 to -13.1 dB, and an average radiation floor of -30.0 to -30.5 dB.

Table 4 summarizes the beam-space performance of deterministic and stochastic dithered DCMs over steering angles from $\pm 10^\circ$ to $\pm 50^\circ$. Increasing the phase resolution generally improves steering accuracy and suppresses parasitic radiation. The most pronounced benefit of SDPQ is observed for the 2-bit DCM, where the steering error is reduced to below 0.8%, the worst parasitic lobe is suppressed, and the QLL improves substantially from $-8.2 \sim -9.9$ dB to $-16.3 \sim -18.6$ dB. The 1-bit DCM is more sensitive to stochastic perturbation and does not exhibit consistent improvement across the evaluated metrics. For the 3- and 4-bit DCMs, SDPQ further reduces the QLL, although the overall benefit becomes less significant because deterministic quantization already provides comparatively accurate beam formation. These results identify the 2-bit DCM as the most favorable regime for SDPQ, providing a strong balance between beam-space improvement and phase-resolution complexity.

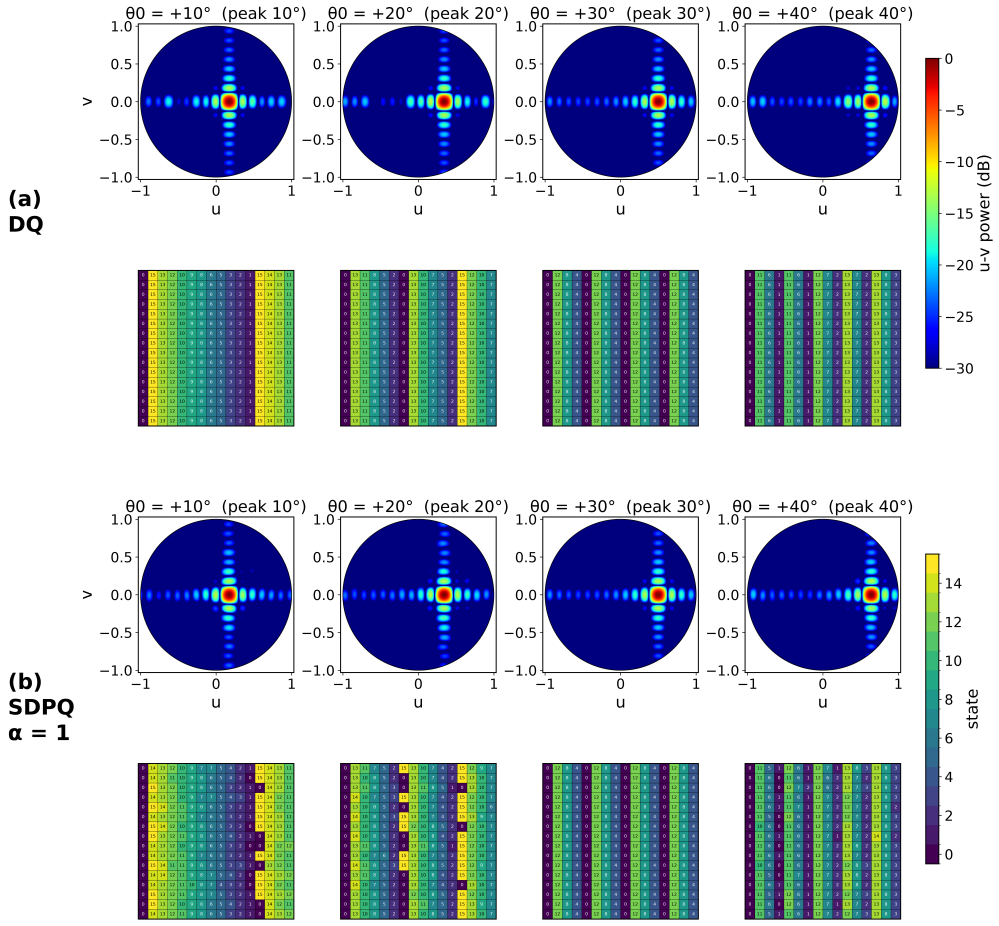


Figure 7. Representative comparison of (**a**) DQ (deterministic) and (**b**) SDPQ (stochastic dithered) beam-space responses and corresponding coding matrices of a 4-bit DCM for E-plane beam steering over scanning angles from $+10^\circ$ to $+40^\circ$.

Table 4. Beam-space performance for deterministic (Det.) and stochastic dithered (SD) multi-bit DCMs over steering angles from $\pm 10^\circ$ to $\pm 50^\circ$.

Bit	Beam Steering Error (%)		Worst Parasitic Lobe (dB)	
	Det.	SD	Det.	SD
1-bit	0.5–3.7	0.5–5.0 †	−6.9 to −11.0	−6.6 to −11.3
2-bit	0–1.9	0–0.8	−7.4 to −13.1	−10.6 to −13.1
3-bit	0–1.6	0–0.9	−9.3 to −13.1	−12.0 to −13.1
4-bit	0–0.9	0–0.8	−11.8 to −13.1	−12.7 to −13.1
Bit	**Mean Radiation Floor (dB)**		**QLL (dB)**	
	Det.	**SD**	**Det.**	**SD**
1-bit	−23.6 to −27.5	−17.1 to −20.4	−6.2 to −12.8	−4.4 to −11.3
2-bit	−26.9 to −30.5	−25.0 to −30.5	−8.2 to −9.9	−16.3 to −18.6
3-bit	−29.3 to −30.5	−28.7 to −30.5	−16.5 to −17.5	−24.3 to −27.0
4-bit	−30.1 to −30.5	−30.0 to −30.5	−23.2 to −24.0	−29.6 to −33.0

† Maximum steering error occurs at 10°; all other cases are $\leq$1.6%. QLL is undefined at $\pm 30^\circ$ for 2–4 bit.

3.1.2. Quantitative Beam-Space Performance Analysis

The beam-space performance of the proposed SDPQ is evaluated using field fidelity (F_{field}), pattern similarity (S_P), sidelobe level (SLL), and steering error. Figure 8 compares DQ ($\alpha = 0$) with SDPQ at $\alpha = 0.5$ and 1.0 for E-plane steering angles of 20° and 40°. Both F_{field} and S_P increase with phase resolution and approach unity for the 3- and 4-bit DCMs. Increasing the dither strength reduces F_{field}, particularly at low phase resolutions,

due to the introduced stochastic phase perturbation. In contrast, the 2-bit DCM maintains near-unity S_P, with SDPQ slightly improving the pattern similarity relative to DQ. This distinction indicates that SDPQ can redistribute structured quantization errors and improve beam-pattern formation even when the complex-field fidelity is reduced.

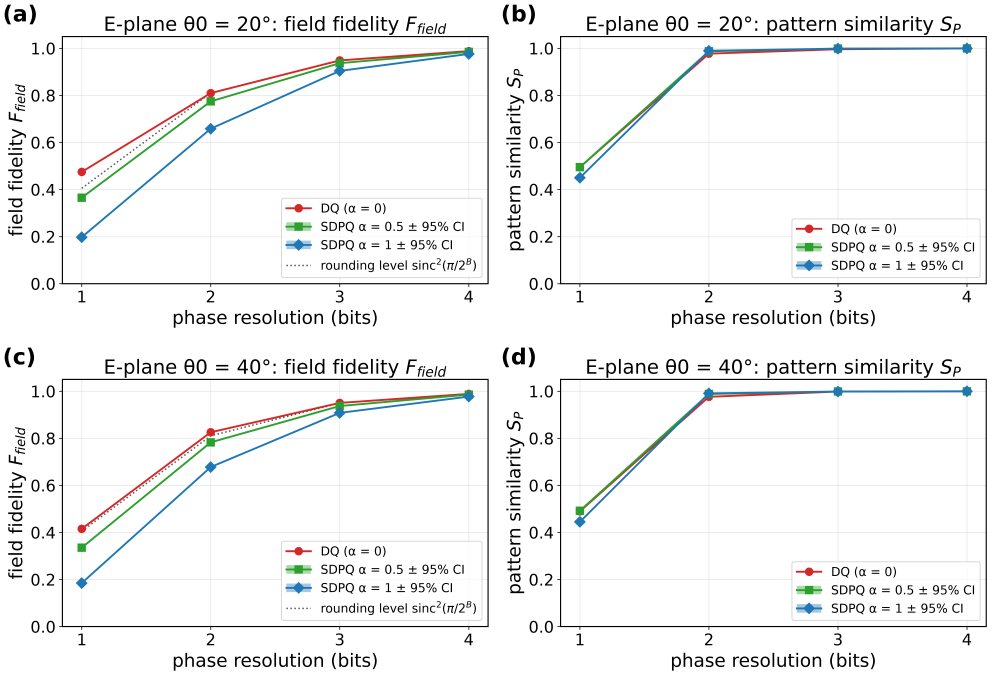


Figure 8. Comparison of field fidelity (F_{field}) and power-pattern similarity (S_P) across 1–4-bit DCMs using DQ, $\alpha = 0$ and SDPQ, $\alpha = 0.5$ and 1.0). (**a**) Field fidelity and (**b**) power-pattern similarity at $\theta_0 = 20°$; (**c**) field fidelity and (**d**) power-pattern similarity at $\theta_0 = 40°$. SDPQ results are presented as mean values with 95% confidence intervals.

Figure 9 illustrates the frequency-dependent beam-space performance of DQ and SDPQ for 1–4-bit DCMs. Both F_{field} and S_P reach their highest values near the 10 GHz design frequency and decrease away from it, with greater frequency sensitivity observed at $\theta_0 = 40°$. SDPQ generally reduces F_{field} because of the introduced stochastic phase perturbation, particularly for the 1- and 2-bit DCMs. However, the 2-bit SDPQ maintains high S_P around the design frequency, approaching the pattern similarity of the 3- and 4-bit DCMs despite its lower phase resolution. The 3- and 4-bit cases remain comparatively robust, with only minor differences between DQ and SDPQ. These results further highlight the 2-bit DCM as a favorable regime for SDPQ, where beam-pattern quality can be preserved despite the reduction in complex- field fidelity.

Tables 5 compares the beam-space performance of deterministic and stochastic dithered phase quantization ($\alpha = 1$) at E-plane steering angles of 20° and 40°. The most pronounced improvement is observed for the 2-bit DCM. At 20°, S_P increases from 0.977 to 0.990, while the SLL improves from −9.49 to −11.80 dB and the QLL from −9.38 to −17.26 dB. Similarly, at 40°, S_P increases from 0.976 to 0.991, with the SLL reduced from −8.22 to −11.83 dB and the QLL from −9.71 to −17.56 dB. These improvements are achieved while preserving steering accuracy, although F_{field} decreases due to the introduced stochastic phase perturbation. In contrast, the 1-bit DCM shows limited and angle-dependent improvement, whereas the 3- and 4-bit DCMs exhibit only marginal changes in SLL because their deterministic beam patterns are already well formed. These results identify the 2-bit DCM as the most favorable phase resolution for exploiting the beam-space benefits of SDPQ.

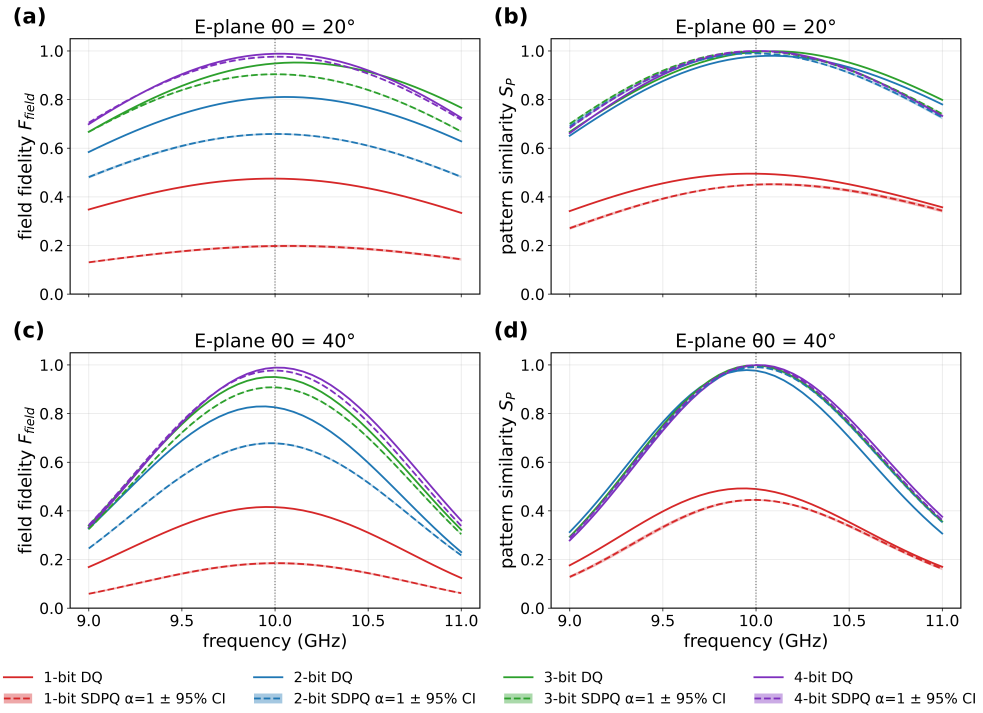


Figure 9. Frequency-dependent beam-space fidelity of 1–4-bit DCMs using DQ and SDPQ, $\alpha = 1.0$ over 9–11 GHz. (**a**) Field fidelity (F_{field}) and (**b**) power-pattern similarity (S_P) at $\theta_0 = 20°$; (**c**) field fidelity and (**d**) power-pattern similarity at $\theta_0 = 40°$. Solid curves represent DQ results, while dashed curves show SDPQ mean values with 95% confidence intervals. The dotted line marks 10 GHz.

Table 5. Comparison of DQ and SDPQ for E-plane steering at $\theta_0 = 20°$ and 40°. SDPQ results ($\alpha = 1$) are reported as the mean of 96 independent realizations.

Bit	Dither	F_{field}	S_P	Steering Error (°)	SLL (dB)	QLL (dB)
			$\theta_0 = 20°$			
1	No	0.475	0.495	0.12	−8.81	−6.80
1	Yes	0.198	0.450	0.26	−8.70	−8.03
2	No	0.810	0.977	0.18	−9.49	−9.38
2	Yes	0.658	0.990	0.17	−11.80	−17.26
3	No	0.949	0.996	0.18	−12.46	−16.55
3	Yes	0.904	0.999	0.14	−12.54	−25.08
4	No	0.988	0.999	0.18	−12.74	−23.19
4	Yes	0.976	1.000	0.14	−12.88	−31.51
			$\theta_0 = 40°$			
1	No	0.415	0.490	0.21	−7.49	−7.92
1	Yes	0.185	0.445	0.35	−8.59	−7.73
2	No	0.826	0.976	0.21	−8.22	−9.71
2	Yes	0.678	0.991	0.20	−11.83	−17.56
3	No	0.950	0.999	0.21	−12.68	−16.90
3	Yes	0.908	0.999	0.19	−12.59	−25.17
4	No	0.989	0.999	0.17	−12.59	−24.02
4	Yes	0.977	1.000	0.18	−12.86	−31.85

3.2. Influence and Optimization of Dither Strength

The influence of the dithering parameter α was investigated for 1-, 2-, 3-, and 4-bit DCMs with an E-plane steering angle of 40°. Four dithering levels ($\alpha = 0$, 0.5, 1.0, and 2.0)

were evaluated by comparing the resulting coding matrices and normalized u–v far-field distributions.

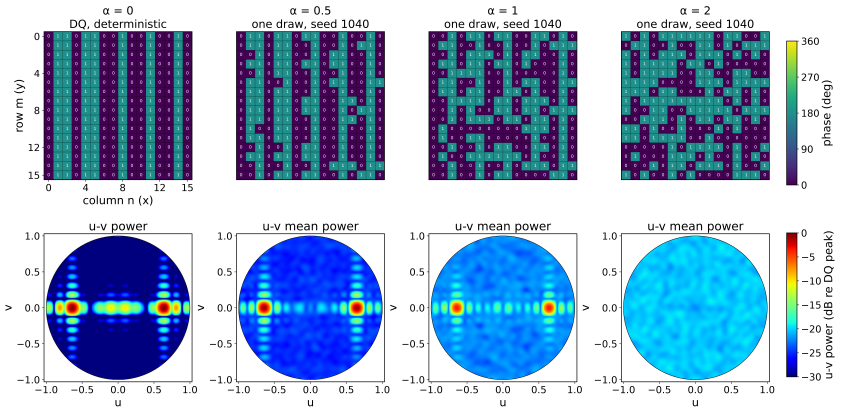
Figure 10b,d highlights the resolution-dependent effect of dithering. The clearest benefit occurs at 2 bits, where moderate dithering suppresses coherent quantization features while retaining the intended beam direction; excessive dithering ($\alpha = 2$) increases diffuse scattering. At 3–4 bits, the smaller quantization error leaves less scope for improvement. Thus, dither strength should balance coherent-artifact suppression against the diffuse background. Since the patterns are peak-normalized, they do not establish changes in absolute gain or beam efficiency.

Tables 6 summarizes the effects of dither strength on field fidelity (F_{field}) and power-pattern similarity (S_P) for E-plane steering at 20° and 40°. Increasing α generally reduces F_{field}, particularly for the 1-bit and 2-bit DCMs, due to the additional stochastic phase perturbation. In contrast, the 2-bit DCM exhibits improved S_P, increasing from 0.977 to 0.990 at 20° and from 0.976 to 0.991 at 40° for $\alpha = 1$. This indicates that SDPQ can improve the power-pattern similarity despite a reduction in complex-field fidelity. The 3- and 4-bit DCMs maintain near-unity S_P over a broad range of α, indicating that dithering provides only limited additional pattern-level benefit at higher phase resolutions.

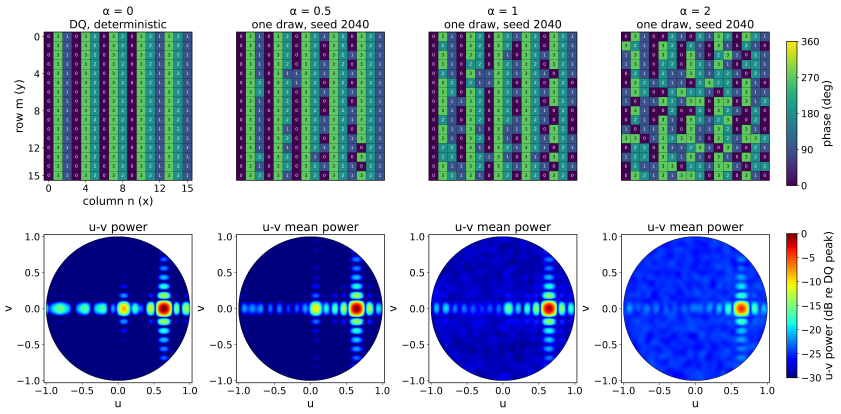
Table 6. Field fidelity (F_{field}) and power-pattern similarity (S_P) versus dither strength for E-plane steering at $\theta_0 = 20°$ and 40°. SDPQ results for $\alpha > 0$ are reported as the mean of 96 independent realizations.

Metric	Bits	$\alpha = 0$	$\alpha = 0.5$	$\alpha = 1.0$	$\alpha = 1.5$	$\alpha = 2.0$
			$\theta_0 = 20°$			
F_{field}	1	0.475	0.365	0.198	0.043	0.004
F_{field}	2	0.810	0.775	0.658	0.504	0.334
F_{field}	3	0.949	0.937	0.904	0.845	0.773
F_{field}	4	0.988	0.985	0.976	0.958	0.936
S_P	1	0.495	0.495	0.450	0.134	0.007
S_P	2	0.977	0.987	0.990	0.976	0.928
S_P	3	0.996	0.999	0.999	0.997	0.995
S_P	4	0.999	1.000	1.000	0.999	0.999
			$\theta_0 = 40°$			
F_{field}	1	0.415	0.335	0.185	0.043	0.005
F_{field}	2	0.826	0.783	0.678	0.499	0.325
F_{field}	3	0.950	0.937	0.908	0.846	0.772
F_{field}	4	0.989	0.986	0.977	0.958	0.936
S_P	1	0.490	0.492	0.445	0.137	0.009
S_P	2	0.976	0.988	0.991	0.976	0.924
S_P	3	0.999	0.999	0.999	0.997	0.995
S_P	4	0.999	1.000	1.000	0.999	0.999

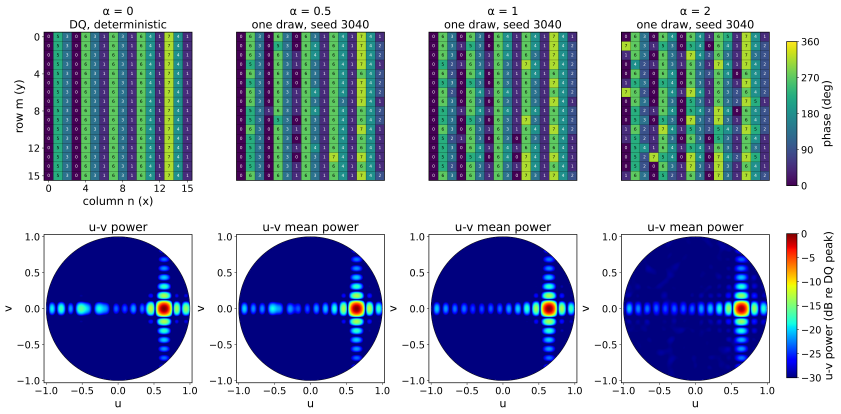
Figure 11a–d systematically evaluates the influence of dither strength α on intended beam efficiency, main-beam loss, worst sidelobe/parasitic level, and mean diffuse floor, respectively. The results reveal a resolution-dependent trade-off between suppression of coherent parasitic radiation and preservation of the intended beam. In general, increasing α redistributes quantization-error energy away from coherent sidelobe structures, but excessive dithering reduces beam efficiency, increases main-beam loss, and raises the diffuse radiation floor. The sensitivity to this trade-off is strongest for the 1-bit DCM, becomes most favorable for the 2-bit DCM, and progressively decreases for the 3- and 4-bit configurations.



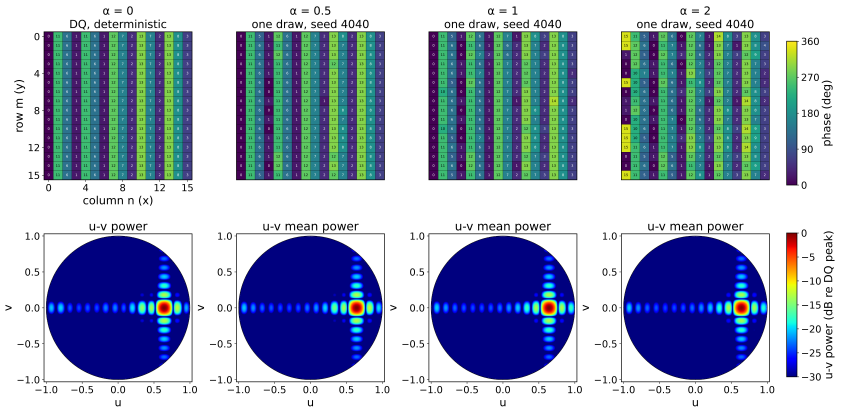
(**a**) 1-bit



(**b**) 2-bit



(**c**) 3-bit



(**d**) 4-bit

Figure 10. Effects of dither strength of DCMs steered toward $\theta_0 = 40°$: (**a**) 1-bit, (**b**) 2-bit, (**c**) 3-bit, and (**d**) 4-bit configurations. For each bit resolution, the upper row shows the phase-coding matrices, while the lower row presents the u–v far-field patterns. The columns compare DQ ($\alpha = 0$) with SDPQ at dither strengths of $\alpha = 0.5$, 1.0, and 2.0.

For the 1-bit DCM, moderate dithering initially suppresses the worst parasitic level, with the most favorable region occurring around $\alpha \approx 0.5$–0.6. However, further increasing α causes rapid beam degradation: the intended beam efficiency decreases substantially, the main-beam loss increases, and the diffuse floor rises sharply. This behavior indicates that the coarse two-state phase representation is highly sensitive to excessive stochastic perturbation. The inherent symmetric twin-beam response of the 1-bit phase coding further limits the achievable benefit.

The 2-bit DCM exhibits a broader and more useful operating region. Increasing α progressively suppresses the worst parasitic level, which reaches its minimum near $\alpha \approx 0.8$–1.0, while the intended beam remains comparatively well preserved. At $\alpha = 1$, the beam efficiency remains approximately 60%, with a main-beam loss of about 1 dB, while the worst parasitic level is reduced to approximately -12 dB. Although the diffuse floor increases moderately, the redistribution of coherent quantization artifacts provides a favorable beam-space trade-off. Accordingly, $\alpha = 1$ is adopted as the reference operating point for the detailed 2-bit SDPQ analysis and subsequent full-wave verification.

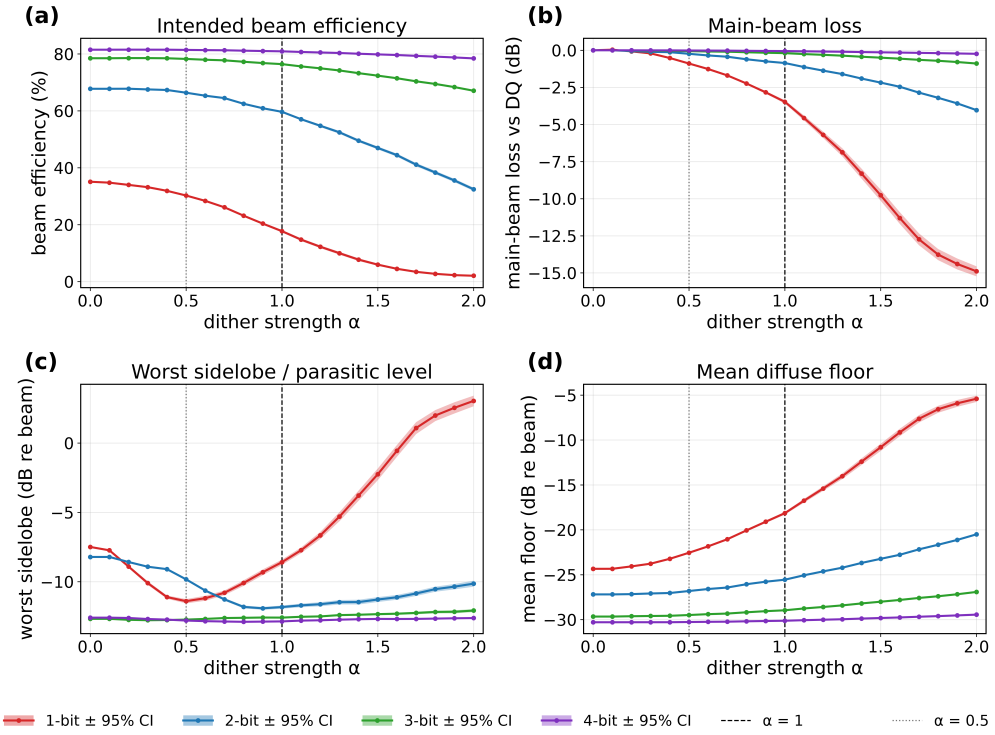


Figure 11. Performance of 1-bit to 4-bit digital coding metasurfaces versus dither strength α. (**a**) Intended beam efficiency, (**b**) main-beam loss, (**c**) worst sidelobe/parasitic level, and (**d**) mean diffuse floor. The dashed line indicates the selected operating point, $\alpha = 1$.

For the 3- and 4-bit DCMs, the intended beam efficiency remains high and the main-beam loss is small over the investigated range of α. However, their worst sidelobe levels change only slightly because the finer phase resolution already provides comparatively accurate deterministic beam formation. Dithering therefore offers limited additional benefit at higher phase resolutions. These observations demonstrate that the appropriate dither strength is resolution dependent, as summarized in Table 7. The 2-bit DCM offers the most favorable trade-off between parasitic-lobe suppression and beam degradation under SDPQ, supporting the adoption of $\alpha = 1.0$ as a common reference rather than a universally optimal dither strength.

Table 7. Resolution-dependent influence and recommended operating range of the SDPQ dither strength.

Bit	Quant. Error	SDPQ Response	High-α Effect	Recommended α
1	High	Strong parasitic-lobe reduction at moderate α; high sensitivity	Severe beam loss and elevated diffuse floor	$\approx$0.5
2	Moderate	Strong and sustained parasitic-lobe suppression	Moderate efficiency loss and increased diffuse floor	$\approx$1.0
3	Low	Limited additional sidelobe improvement	Small beam-efficiency and main-beam loss	$\lesssim$0.5
4	Very low	Negligible additional sidelobe improvement	Minimal beam degradation	$\lesssim$1.0

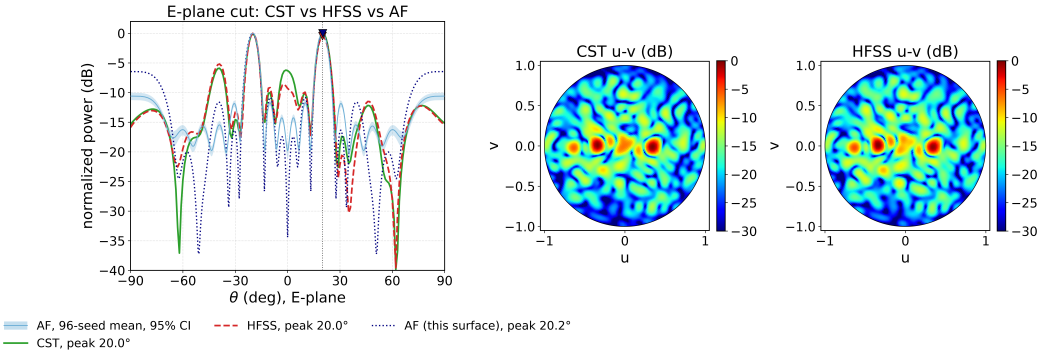
3.3. Full-Wave Electromagnetic Verification

To verify the proposed stochastic dithered phase quantization framework, full-wave electromagnetic simulations were conducted using CST Microwave Studio [55], which employs a time-domain solver, and Ansys HFSS [56], which is based on the finite element method (FEM). The full-wave simulation configurations used for electromagnetic verification are summarized in Table 8. Using the height-step DCM reflector described in Section 2.3, the analytical array-factor (AF) predictions were validated against the radiation characteristics of the stochastic dithered 1-, 2-, 3-, and 4-bit DCMs at E-plane steering angles of 20° and 40°, as shown in Figures 12 and 13, respectively. The comparisons include the normalized radiation patterns and two-dimensional beam-space distributions obtained from the AF, CST, and HFSS models.

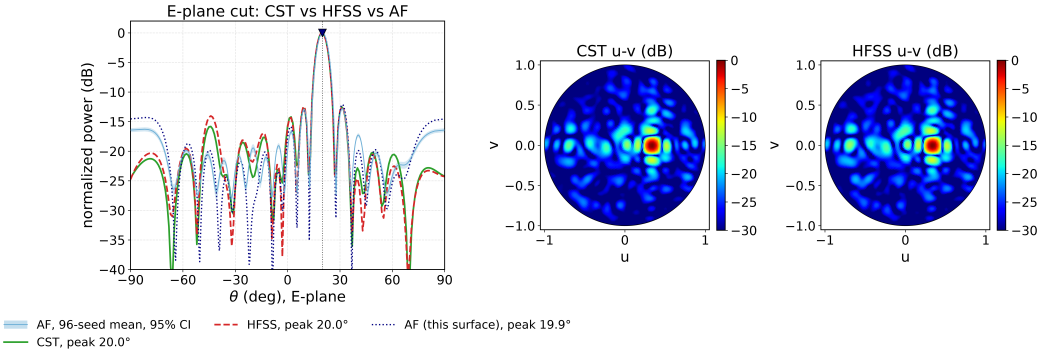
Excellent agreement is observed between the analytical and full-wave results across all phase resolutions and steering angles. The AF model accurately predicts the main-beam direction, sidelobe characteristics, and beam-space distributions, demonstrating its capability to represent the stochastic dithered DCMs. Even for the 1-bit DCM, where phase quantization is most severe, the analytical predictions closely match the CST and HFSS simulations. As the phase resolution increases from 2 to 4 bits, the agreement becomes progressively stronger owing to the reduced quantization error, with the 4-bit DCM exhibiting nearly identical AF, CST, and HFSS radiation patterns. These results validate the proposed analytical beam synthesis model and confirm the effectiveness of the SDPQ framework for accurately predicting the radiation behavior of multi-bit digital coding metasurfaces.

Table 8. Full-wave simulation setup of the height-step DCM reflectors.

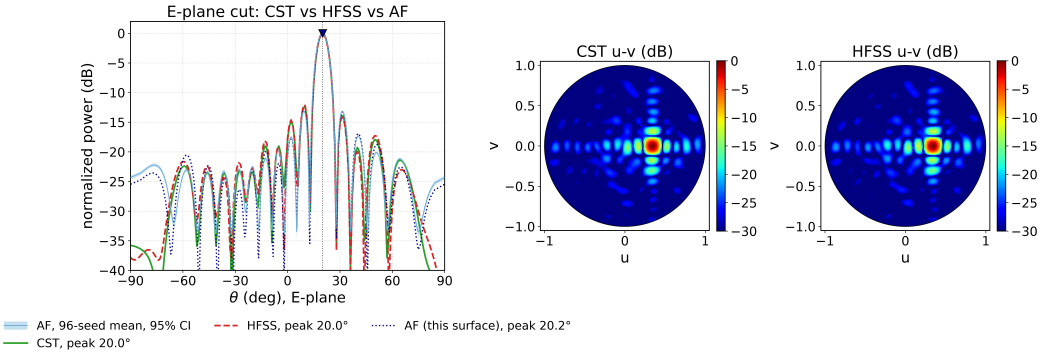
Parameter	CST	HFSS
Frequency	10 GHz	10 GHz
Unit-cell period	$\lambda_0/2$ = 14.99 mm	$\lambda_0/2$ = 14.99 mm
Excitation	Plane wave, normal incidence	Plane wave, normal incidence
Solver	Time domain	FEM (frequency domain)
Mesh	Hexahedral, $\geq$15 cells/λ	Adaptive tetrahedral, $\Delta S \leq 0.015$
Boundary	Open (add space)	Radiation, λ_0 padding
Output	Far-field, 1° step	Far-field, 1° step



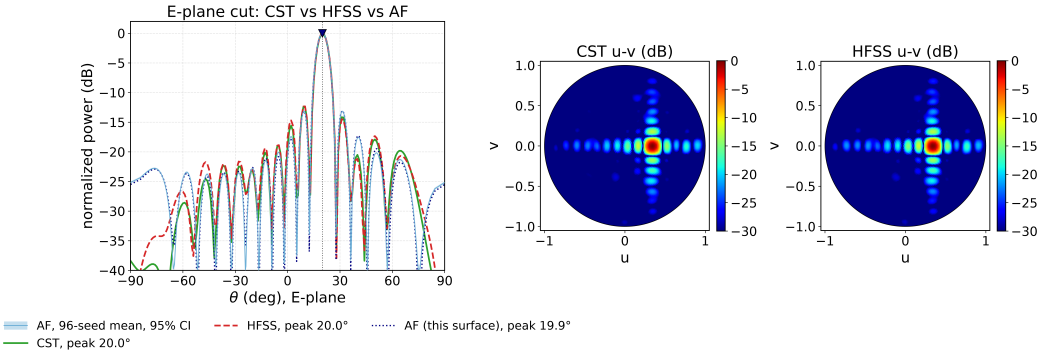
(**a**) 1-bit with dithering at 20°.



(**b**) 2-bit with dithering at 20°.

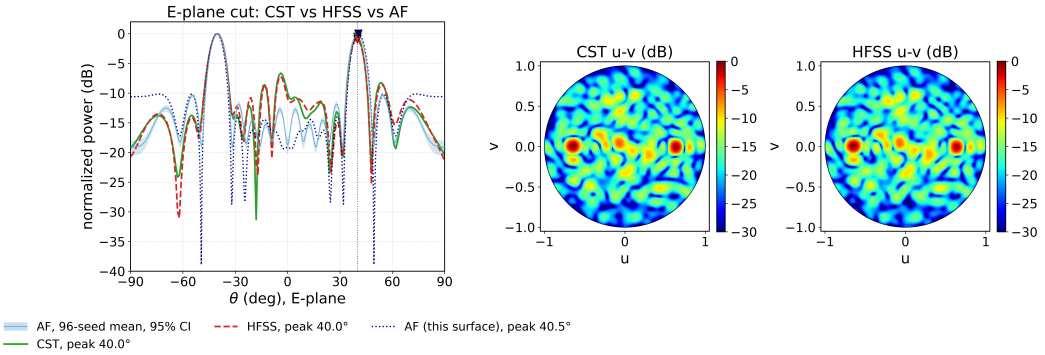


(**c**) 3-bit with dithering at 20°.

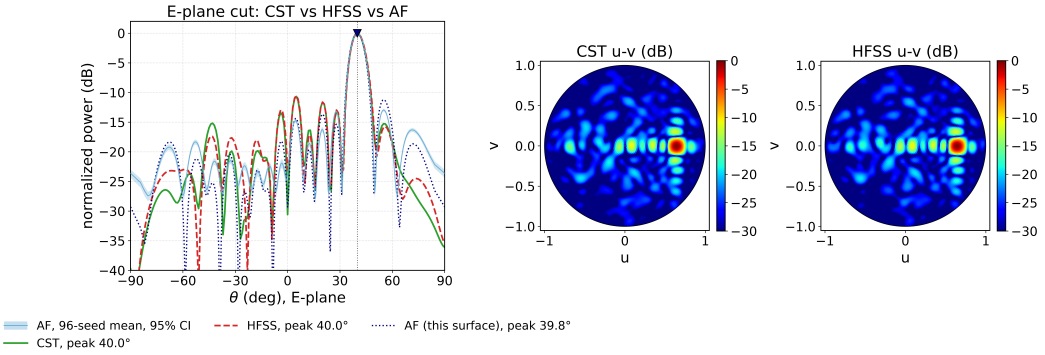


(**d**) 4-bit with dithering at 20°.

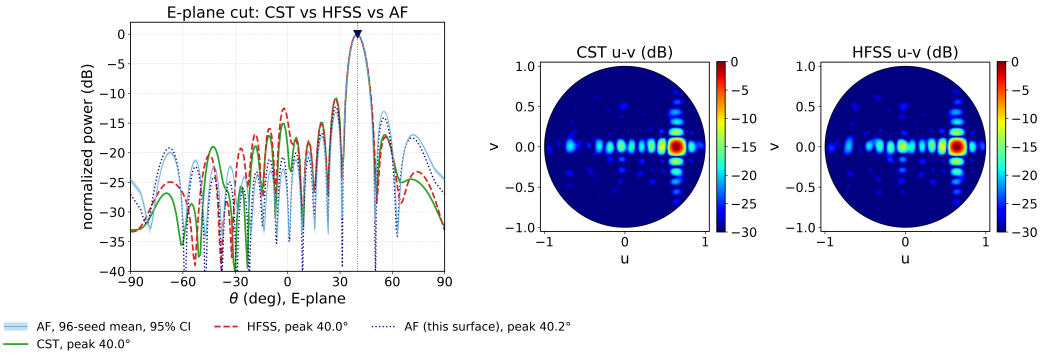
Figure 12. Validation of the analytical array factor (AF) against CST and HFSS full-wave radiation patterns for the proposed SDPQ ($\alpha = 1$) of (**a**) 1-bit, (**b**) 2-bit, (**c**) 3-bit, and (**d**) 4-bit DCMs at an E-plane steering angle of 20°.



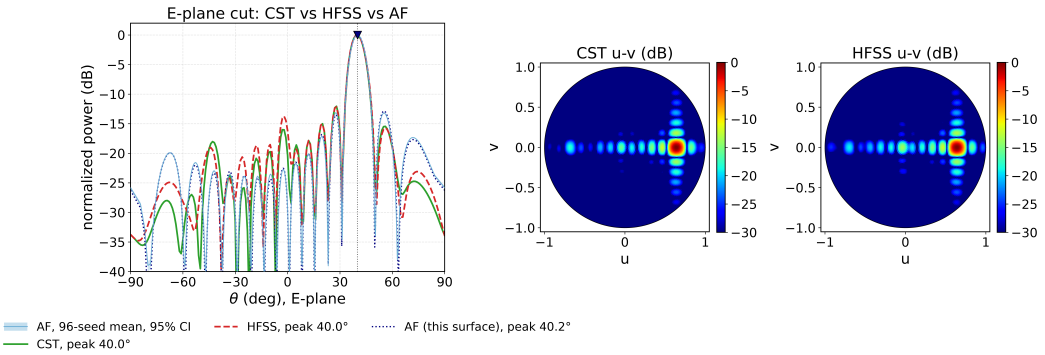
(**a**) 1-bit with dithering at 40°.



(**b**) 2-bit with dithering at 40°.



(**c**) 3-bit with dithering at 40°.



(**d**) 4-bit with dithering at 40°.

Figure 13. Validation of the analytical array factor (AF) against CST and HFSS full-wave radiation patterns for the proposed SDPQ ($\alpha = 1$) of (**a**) 1-bit, (**b**) 2-bit, (**c**) 3-bit, and (**d**) 4-bit DCMs at an E-plane steering angle of 40°.

The full-wave comparisons reveal a strong dependence of SDPQ performance on phase resolution at the reference dither strength $\alpha = 1$. Table 9 summarizes the change in sidelobe level relative to deterministic quantization, defined as $\Delta\text{SLL} = \text{SLL}_{\text{SDPQ}} - \text{SLL}_{\text{DQ}}$. Negative values indicate sidelobe suppression, whereas positive values indicate an increase in sidelobe level.

The clearest improvement is observed for the 2-bit DCM. At $\theta_0 = 20^\circ$, SDPQ reduces the SLL by 3.0 dB in CST and 3.4 dB in HFSS. At $\theta_0 = 40^\circ$, the corresponding reductions are 4.5 and 4.3 dB. The consistent direction and comparable magnitude of these changes across the two solvers support the effectiveness of SDPQ for sidelobe suppression in the investigated 2-bit configurations. Together with the AF–full-wave comparisons, these results support the predicted redistribution of coherent quantization artifacts.

For the 1-bit DCM, both solvers predict increased sidelobe levels at $\alpha = 1$. The increases are 2.3 and 3.3 dB at 20°, and 2.3 and 1.3 dB at 40°, in CST and HFSS, respectively. These results show that the reference dither strength does not provide sidelobe suppression for the investigated two-state reflectors. The analytical parameter sweep suggests that a weaker dither strength, approximately $\alpha = 0.5$, offers a more favorable operating region; however, this alternative requires separate full-wave verification.

For the 3-bit DCM, the SLL increases by 0.5–1.3 dB across the investigated cases, indicating that $\alpha = 1$ provides no sidelobe improvement. For the 4-bit DCM, the changes are limited to 0–0.2 dB, indicating little sensitivity to dithering in this comparison. These findings are consistent with the diminishing opportunity to suppress quantization artifacts as deterministic phase resolution increases.

The verification therefore supports a resolution-dependent application of SDPQ. Agreement between the AF and full-wave patterns assesses the predictive capability of the analytical model, while the DQ–SDPQ comparison establishes whether dithering improves the selected performance metric. Among the full-wave configurations examined at $\alpha = 1$, the 2-bit DCM provides the clearest sidelobe suppression. This conclusion is restricted to the investigated reflector geometries, steering angles, and simulation conditions; it does not establish optimal dither strengths for all resolutions or robustness to fabrication errors.

Table 9. SDPQ–DQ SLL changes at $\alpha = 1$ (dB, CST/HFSS). Negative values indicate suppression; positive values indicate an increase.

Resolution	Full-Wave Observation	ΔSLL at 20° CST/HFSS	ΔSLL at 40° CST/HFSS
1-bit	Increased sidelobe level	+2.3 / +3.3	+2.3 / +1.3
2-bit	Consistent sidelobe suppression	−3.0 / −3.4	−4.5 / −4.3
3-bit	Modest increase in sidelobe level	+0.5 / +0.6	+1.3 / +0.8
4-bit	Minimal change in sidelobe level	+0.2 / 0.0	0.0 / +0.2

To contextualize the proposed approach, Table 10 compares the reported SLL and QLL values of SDPQ with the optimized pre-phasing design of Kim et al. [30]. Two-bit SDPQ uses four physical phase states, whereas 3-bit SDPQ and the $K = 4$ pre-phasing design use eight. The reported 3-bit SDPQ QLL values fall within Kim et al.'s range, while their design reports lower SLLs. Kim et al. provide simulation and experimental validation, whereas SDPQ is evaluated through analytical and full-wave simulations. Differences in aperture size, operating frequency, steering angles, and metric definitions prevent a direct performance ranking.

Table 10. Reported analytical SLL and QLL values for SDPQ and pre-phasing under their respective study conditions.

Method	Physical Phase States	Steering Angle	SLL (dB)	QLL (dB)
2-bit SDPQ, $\alpha = 1$	4	20°	−11.80	−17.26
2-bit SDPQ, $\alpha = 1$	4	40°	−11.83	−17.56
3-bit SDPQ, $\alpha = 1$	8	20°	−12.54	−25.08
3-bit SDPQ, $\alpha = 1$	8	40°	−12.59	−25.17
[30], $K = 4$ pre-phasing	8	15°	−14.80	−22.40
[30], $K = 4$ pre-phasing	8	30°	−15.50	−24.40
[30], $K = 4$ pre-phasing	8	45°	−14.90	−25.50

SDPQ results are ensemble means over 96 realizations for a 16 × 16 aperture at 10 GHz. Pre-phasing results are taken from Table I of [30] for a 30 × 30 aperture at 140 GHz.

4. Conclusions

This paper presents SDPQ for 1–4-bit DCMs using array-factor analysis and CST/HFSS simulations of height-step reflectors. The results show that spatial redistribution of quantization errors produces resolution- and strength-dependent trade-offs between coherent-lobe suppression, diffuse scattering, and beam preservation.

The strongest demonstrated benefit occurs in the investigated 2-bit configurations, which retain four physical phase states. Compared with DQ, SDPQ reduced the worst-case parasitic-lobe level from −7.4 to −10.6 dB and the maximum steering error from 1.9% to 0.8%. Power-pattern similarity improved, and QLL decreased, although complex-field fidelity declined. At $\alpha = 1$, full-wave simulations confirmed SLL reductions of 3.0–3.4 dB at 20° and 4.3–4.5 dB at 40°.

For ideal equal-amplitude 1-bit DCMs, dithering does not remove the inherent symmetric twin beams, and excessive perturbation weakens beam concentration. For 3–4-bit DCMs, higher phase accuracy leaves limited scope for additional improvement. These findings support 2-bit SDPQ as a useful low-bit option under the studied conditions, with dither strength chosen to balance artifact suppression and beam preservation.

Future work will prioritize experimental validation, including fabrication tolerances, amplitude nonuniformity, material losses, and mutual coupling. Further directions include adaptive dithering, learning-assisted synthesis, and extensions to RIS, multibeam, and wideband operation.

Author Contributions: Conceptualization, T.T., K.K., and P.C.; methodology, T.T., K.K., and P.C.; software, T.T.; validation, T.T., K.K., and P.C.; formal analysis, T.T.; investigation, T.T.; writing—original draft preparation, T.T. and K.K.; writing—review and editing, T.T., K.K., and P.C.; visualization, T.T.; supervision, K.K. and P.C. All authors have read and agreed to the published version of the manuscript.

Funding: This research received no external funding.

Institutional Review Board Statement: Not applicable

Informed Consent Statement: Not applicable

Data Availability Statement: The data supporting the findings of this study are available from the corresponding author upon reasonable request.

Acknowledgments: The authors gratefully acknowledge the Faculty of Engineering, Prince of Songkla University, Thailand, for providing the Engineering Graduate Scholarship that supported this work.

Conflicts of Interest: The authors declare no conflicts of interest.

Appendix A. Aperture Phase-Error Characterization

Appendix A.1. Phase-Quantized Profiles

Figure A1 compares ideal, deterministic, and SDPQ phase profiles for a 16-element linear phase-gradient sequence with 1–4-bit coding. Higher resolution more closely approximates the ideal profile. Deterministic quantization produces correlated errors and coherent quantization lobes, especially at low resolutions. SDPQ adds zero-mean uniform dither before nearest-state quantization, following Equation (3). The reference setting $\alpha = 1$ provides a dither range of $[-\Delta/2, \Delta/2]$, where Δ is the quantization interval.

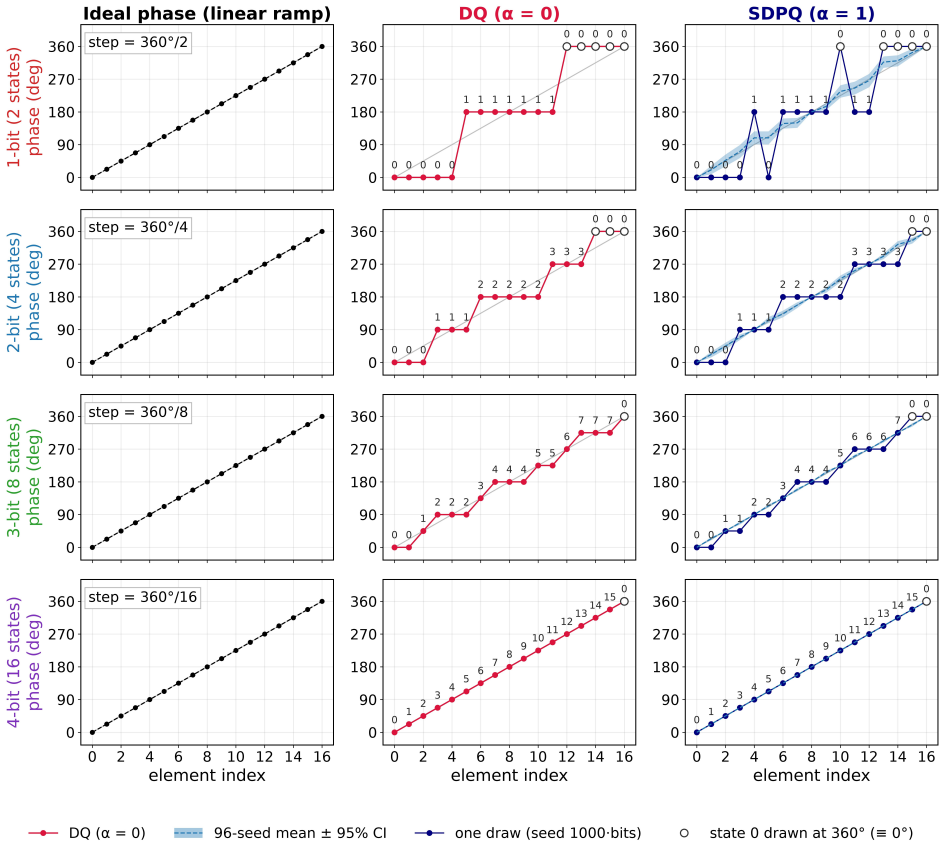


Figure A1. Comparison of ideal continuous phase, deterministic phase quantization, and stochastic dithered phase quantization for 1-, 2-, 3-, and 4-bit DCMs.

Figure A1 shows that dithering disrupts regular phase-state patterns mainly at 1–2 bits while preserving the overall gradient; changes are smaller at 3 bits and negligible at 4 bits. Rather than minimizing instantaneous phase error, SDPQ reduces its spatial correlation, redistributing coherent quantization lobes into diffuse scattering.

Appendix A.2. Phase Error Analysis

Figure A1 compares ideal, deterministic, and dithered phase profiles for a 16-element sequence. The phase error is

$$e_i = \phi_i^{(\mathrm{q})} - \phi_i^{(\mathrm{ideal})}, \tag{A1}$$

where $\phi_i^{(\mathrm{q})}$ is the deterministic or dithered phase. For N elements, the error metrics are

$$\mathrm{MAE} = \frac{1}{N}\sum_{i=1}^{N} |e_i|, \qquad \mathrm{RMSE} = \sqrt{\frac{1}{N}\sum_{i=1}^{N} e_i^2}. \tag{A2}$$

Table A1 shows lower errors for deterministic quantization at 1–2 bits, similar results at 3 bits, and negligible errors at 4 bits. Since SDPQ targets spatial error decorrelation rather than minimum phase error, its effectiveness is further assessed using beam-space metrics.

Table A1. Phase-error statistics relative to the ideal continuous phase profile (dithered: the mean of 96 independent realizations).

Bit	Method	MAE (°)	RMSE (°)	Max Error (°)
1	Deterministic	42.35	51.19	90.0
1	Dithered	54.82	69.21	157.5
2	Deterministic	21.18	26.73	45.0
2	Dithered	26.31	34.01	67.5
3	Deterministic	10.59	15.43	22.5
3	Dithered	10.59	15.43	22.5
4	Deterministic	0.00	0.00	0.0
4	Dithered	0.00	0.00	0.0

Algorithm 1 generates deterministic or dithered coding sequences, shown in Figures A2 and A3 for 20° and 40° steering at 1–4 bits. Higher resolution improves phase accuracy, while dithering reduces spatial error correlation and preserves the overall phase gradient.

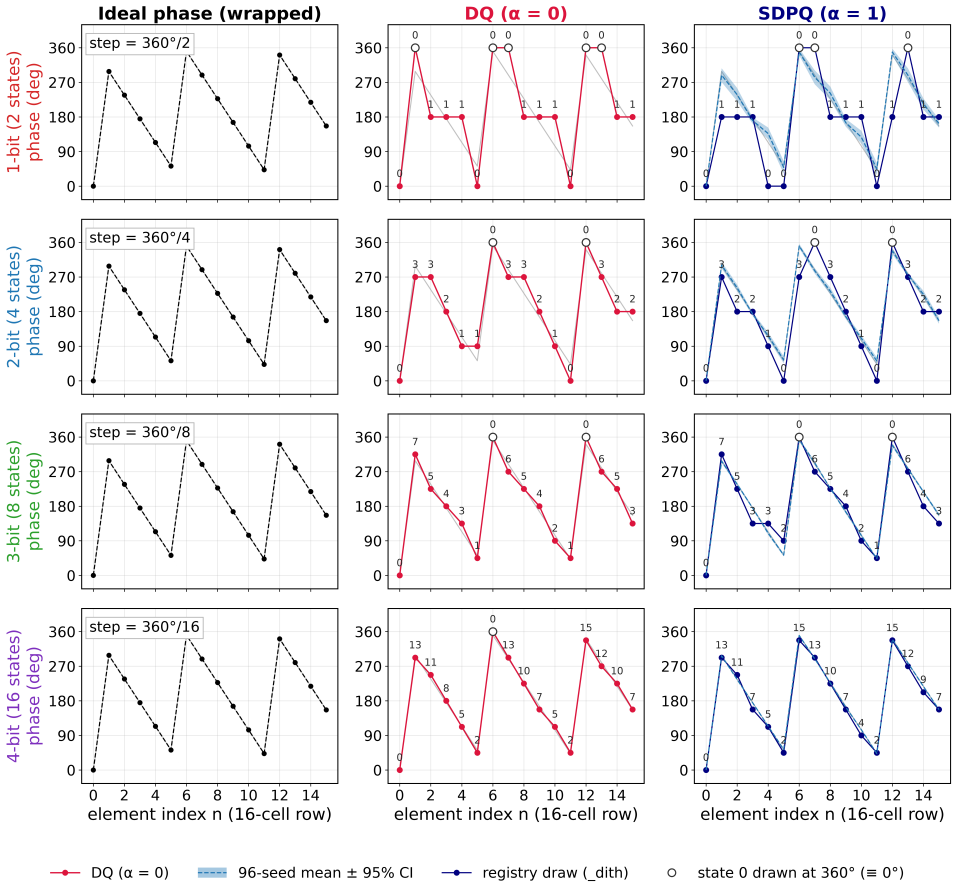


Figure A2. Ideal, deterministic, and dithered phase profiles for 1–4-bit DCMs steered to 20°.

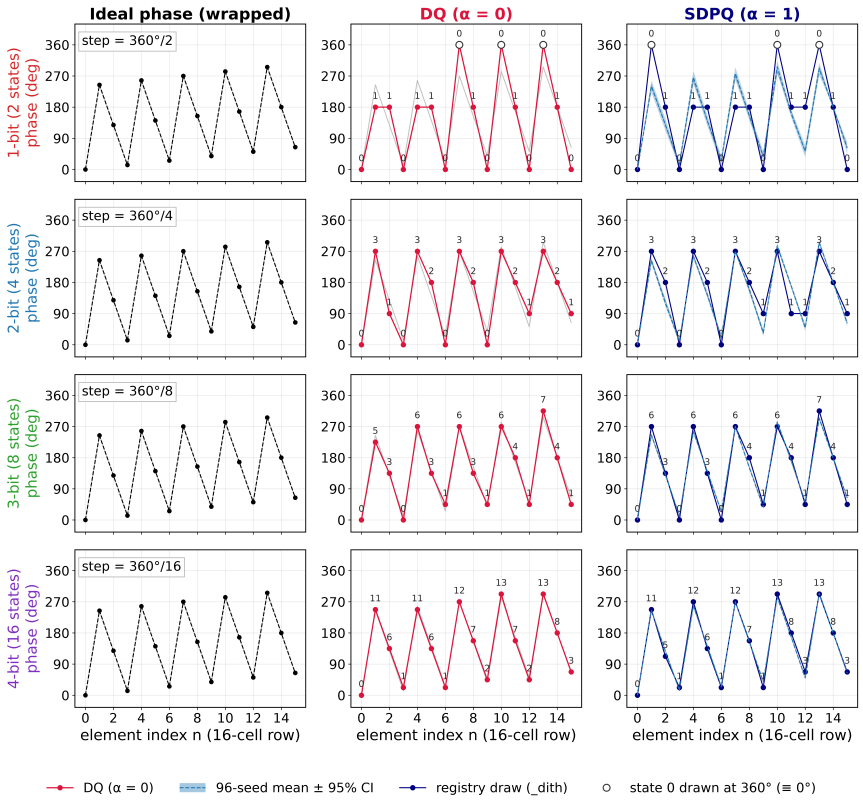


Figure A3. Ideal, deterministic, and dithered phase profiles for 1–4-bit DCMs steered to 40°.

Figures A2 and A3 compare ideal, deterministic, and dithered phase sequences for a 16-element metasurface steered to 20° and 40°. The steeper 40° gradient produces more phase wrapping. Deterministic errors are spatially correlated, particularly at 1–2 bits, while dithering reduces this correlation and preserves the overall gradient. Both methods approach the ideal profile as resolution increases to 4 bits.

Appendix A.3. Phase Error for Beam Steering at 20° and 40°

Table A2 compares MAE and RMSE at 20° and 40°. Deterministic quantization provides lower errors, particularly at 1–2 bits, while both methods converge at higher resolutions. SDPQ is further assessed using radiation patterns, steering accuracy, SLL, field fidelity (F_{field}), and power-pattern similarity (S_P).

Table A2. Estimated phase-error statistics for deterministic and stochastic dithered quantization under different E-plane steering angles (Dithered: the mean of 96 independent realizations).

Bit	Method	$\theta = 20°$			$\theta = 40°$		
		MAE (°)	RMSE (°)	Max (°))	MAE (°))	RMSE (°)	Max (°)
1	Deterministic	41.4	48.8	90	43.4	51.4	90
	Dithered	56.4	71.2	180	57.4	71.8	180
2	Deterministic	22.5	26.1	45	20.9	24.9	45
	Dithered	30.0	36.7	90	28.0	35.5	90
3	Deterministic	11.3	13.1	22.5	10.9	13.0	22.5
	Dithered	14.8	18.2	45	14.2	17.8	45
4	Deterministic	5.3	6.3	11.25	5.0	6.1	11.25
	Dithered	7.1	8.9	22.5	6.8	8.7	22.5

Table A3 shows the additional MAE and RMSE from dithering, largest at 1 bit and slightly higher at 40°. The increase decreases with resolution and is negligible at 4 bits.

Table A3. Increase in phase error introduced by stochastic dithering relative to deterministic quantization.

Bit	$\theta = 20°$		$\theta = 40°$	
	ΔMAE (°)	**ΔRMSE (°)**	**ΔMAE (°)**	**ΔRMSE (°)**
1	15.0	22.4	14.0	20.4
2	7.5	10.6	7.1	10.6
3	3.5	5.1	3.3	4.8
4	1.8	2.6	1.8	2.6

References

1. Cui, T.J.; Qi, M.Q.; Wan, X.; Zhao, J.; Cheng, Q. Coding metamaterials, digital metamaterials and programmable metamaterials. *Light Sci. Appl.* **2014**, *3*, e218. https://doi.org/10.1038/lsa.2014.99.
2. Liu, S.; Cui, T.J.; Xu, Q.; Bao, D.; Du, L.; Wan, X.; Tang, W.X.; Ouyang, C.; Zhou, X.Y.; Yuan, H.; et al. Anisotropic coding metamaterials and their powerful manipulation of differently polarized terahertz waves. *Light Sci. Appl.* **2016**, *5*, e16076. https://doi.org/10.1038/lsa.2016.76.
3. Wan, X.; Qi, M.Q.; Chen, T.Y. Field-programmable beam reconfiguring based on digitally controlled coding metasurface. *Sci. Rep.* **2016**, *6*, 20663. https://doi.org/10.1038/srep20663.
4. Zhang, L.; Chen, X.Q.; Liu, S.; Zhang, Q.; Zhao, J.; Dai, J.Y.; Bai, G.D.; Wan, X.; Cheng, Q.; Castaldi, G.; et al. Space-time-coding digital metasurfaces. *Nat. Commun.* **2018**, *9*, 4334. https://doi.org/10.1038/s41467-018-06802-0.
5. Zhang, X.G.; Tang, W.X.; Jiang, W.X.; Bai, G.D.; Tang, J.; Bai, L.; Qiu, C.-W.; Cui, T.J. Light-controllable digital coding metasurfaces. *Adv. Sci.* **2018**, *5*, 1801028. https://doi.org/10.1002/advs.201801028.
6. Cui, T.J.; Li, L.; Liu, S.; Ma, Q.; Zhang, L.; Wan, X.; Jiang, W.X.; Cheng, Q. Information metamaterial systems. *iScience* **2020**, *23*, 101403. https://doi.org/10.1016/j.isci.2020.101403.
7. Zhang, L.; Cui, T.J. Space-time-coding digital metasurfaces: Principles and applications. *Research* **2021**, *2021*, 9802673. https://doi.org/10.34133/2021/9802673.
8. Ma, Q.; Xiao, Q.; Hong, Q.R.; Gao, X.; Galdi, V.; Cui, T.J. Digital coding metasurfaces: From theory to applications. *IEEE Antennas Propag. Mag.* **2022**, *64*, 96–109. https://doi.org/10.1109/MAP.2022.3169397.
9. Jiang, R.Z.; Ma, Q.; Gu, Z.; Liang, J.C.; Xiao, Q.; Cheng, Q.; Cui, T.J. Simultaneously intelligent sensing and beamforming based on an adaptive information metasurface. *Adv. Sci.* **2024**, *11*, 2306181. https://doi.org/10.1002/advs.202306181.
10. Qian, C.; Kaminer, I.; Chen, H. A guidance to intelligent metamaterials and metamaterials intelligence. *Nat. Commun.* **2025**, *16*, 1154. https://doi.org/10.1038/s41467-025-56122-3.
11. Kasahara, Y.; Alù, A. Microwave metasurfaces. *IEEE Microw. Mag.* **2026**, *27*, 80–97. https://doi.org/10.1109/MMM.2026.3660939.
12. Chen, W.; Liu, J.; Xiu, X.; Tang, K.; Feng, W.; Che, W. Multi-Bit Phase-Coded Metamaterial with Honeycomb EM Structure for Scattering Manipulation Using Deep Learning-Based Method. *IEEE Trans. Microw. Theory Techn.* **2025**, *73*, 7041–7054. https://doi.org/10.1109/TMTT.2025.3574674.
13. Zhang, L.; Wang, Z.X.; Shao, R.W.; Shen, J.L.; Chen, X.Q.; Wan, X.; Cheng, Q.; Cui, T.J. Dynamically Realizing Arbitrary Multi-Bit Programmable Phases Using a 2-Bit Time-Domain Coding Metasurface. *IEEE Trans. Antennas Propag.* **2020**, *68*, 2984–2992. https://doi.org/10.1109/TAP.2019.2955219.
14. Zhang, Y.; Xie, B.; Liu, W.; Cheng, H.; Chen, S.; Tian, J. Anomalous reflection and vortex beam generation by multi-bit coding acoustic metasurfaces. *Appl. Phys. Lett.* **2019**, *114*, 091905. https://doi.org/10.1063/1.5087636.
15. Wang, H.L.; Zhang, Y.K.; Zhang, T.Y.; Ma, H.F.; Cui, T.J. Broadband and programmable amplitude-phase-joint-coding information metasurface. *ACS Appl. Mater. Interfaces* **2022**, *14*, 29431–29440. https://doi.org/10.1021/acsami.2c05907.
16. Ahmed, F.; Hassan, T.; Melouki, N.; Naseri, H.; PourMohammadi, P.; Iqbal, A. A Multibit and Frequency-Reconfigurable Reflecting Surface for RIS Applications. *IEEE Antennas Wirel. Propag. Lett.* **2024**, *23*, 653–657. https://doi.org/10.1109/LAWP.2023.3331608.
17. Kashyap, B.G.; Theofanopoulos, P.C.; Cui, Y.; Trichopoulos, G.C. Mitigating Quantization Lobes in mmWave Low-Bit Reconfigurable Reflective Surfaces. *IEEE Open J. Antennas Propag.* **2020**, *1*, 604–614. https://doi.org/10.1109/OJAP.2020.3034049.
18. Gholami, M.; Khajavi, S.; Neshat, M.; Tewes, S.; Sezgin, A. Realization of Reconfigurable Intelligent Surfaces with Space–Time-Coded Metasurfaces. *IEEE Trans. Antennas Propag.* **2026**, *74*, 4281–4291. https://doi.org/10.1109/TAP.2026.3660044.
19. Marasco, I.; Cantore, C.; Bianco, G.V.; Bruno, G.; D'Orazio, A.; Magno, G. Transparent Graphene-Based RIS for 6G Communications in the THz Spectrum. *IEEE Open J. Antennas Propag.* **2025**, *6*, 193–200. https://doi.org/10.1109/OJAP.2024.3487793.

20. Wang, T.; Teng, Y.; Li, C.; Huang, Z.; Liang, L.; Zhang, Y.; Yao, H.; Jiang, L. A Liquid-Crystal-Based Programmable Metasurface for Full-Space Terahertz Beam Steering. *J. Appl. Phys.* **2025**, *138*, 033105.
21. Xu, L.; Jiang, Z.; Zhang, G.; Yang, C.; Yang, J.; Yin, Z.; Zhong, M.; Lu, H.; Deng, G.; Li, Y. Liquid-Crystal-Based Reconfigurable Intelligent Surface for Sub-Terahertz Wireless Communications. *IEEE Internet Things J.* **2025**, *12*, 37471–37481. https://doi.org/10.1109/JIOT.2025.3583923.
22. Chepuri, S.P.; Shlezinger, N.; Liu, F.; Alexandropoulos, G.C.; Buzzi, S.; Eldar, Y.C. Integrated Sensing and Communications with Reconfigurable Intelligent Surfaces: From Signal Modeling to Processing. *IEEE Signal Process. Mag.* **2023**, *40*, 41–62. https://doi.org/10.1109/MSP.2023.3279986.
23. Zhang, J.A.; Wu, K.; Di Renzo, M.; Cui, T.J. RIS-Enabled Integrated Sensing and Communications: From Theory to Practice. *Proc. IEEE* **2026**, *114*, 121–157. https://doi.org/10.1109/JPROC.2026.3678371.
24. Yang, H.; Yang, F.; Xu, S.; Li, M.; Cao, X.; Gao, J.; Zheng, Y. A study of phase quantization effects for reconfigurable reflectarray antennas. *IEEE Antennas Wirel. Propag. Lett.* **2017**, *16*, 302–305. https://doi.org/10.1109/LAWP.2016.2574118.
25. Wu, Q.; Long, X.; Yin, J.; Yu, C.; Wang, H.; Hong, W. Single-Layer 1-Bit Prephased Single-Beam Metasurface Using True-Time Delayed Unit Cells. *IEEE Antennas Wirel. Propag. Lett.* **2022**, *21*, 1095–1099. https://doi.org/10.1109/LAWP.2022.3157903.
26. Nadi, M.; Sedighy, S.H.; Cheldavi, A. Multimode OAM Beam Generation Through 1-Bit Programmable Metasurface Antenna. *Sci. Rep.* **2023**, *13*, 15603. https://doi.org/10.1038/s41598-023-42691-0.
27. Malleboina, R.; Dash, J.C.; Sarkar, D. Design of Anomalous Reflectors by Phase Gradient Unit Cell-Based Digitally Coded Metasurface. *IEEE Antennas Wirel. Propag. Lett.* **2023**, *22*, 2305–2309. https://doi.org/10.1109/LAWP.2023.3287031.
28. Sang, J.; Lan, J.; Zhou, M.; Gao, B.; Tang, W.; Li, X.; Yi, X.; Jin, S. Quantized Phase Alignment by Discrete Phase Shifts for Reconfigurable Intelligent Surface-Assisted Communication Systems. *IEEE Trans. Veh. Technol.* **2024**, *73*, 5259–5275. https://doi.org/10.1109/TVT.2023.3332107.
29. Narayanan, S.S.; Khankhoje, U.K.; Ganti, R.K. Optimum Beamforming and Grating-Lobe Mitigation for Intelligent Reflecting Surfaces. *IEEE Trans. Antennas Propag.* **2024**, *72*, 8540–8553. https://doi.org/10.1109/TAP.2024.3463805.
30. Kim, T.; Lee, S.; Oh, S.; Kim, J.; Oh, J.; Choi, S. Pre-Phased 1-Bit Reflective Passive Metasurface with Optimum Number of Pre-Phasing for Low QLL and SLL at 140 GHz. *IEEE Trans. Antennas Propag.* **2025**, *73*, 975–985. https://doi.org/10.1109/TAP.2024.3510861.
31. Shekhawat, A.S.; Kashyap, B.G.; Raldiris Torres, R.W.; Shan, F.; Trichopoulos, G.C. A Millimeter-Wave Single-Bit Reconfigurable Intelligent Surface with High-Resolution Beam-Steering and Suppressed Quantization Lobe. *IEEE Open J. Antennas Propag.* **2025**, *6*, 311–325. https://doi.org/10.1109/OJAP.2024.3506453.
32. Yu, H.; Pan, Z.; Qu, M.; Su, J.; Yang, L.; Nayyeri, V. Reconfigurable Omni-Metasurface for Single-Beam Steering Based on Simultaneous Transmission–Reflection Continuous Pre-Phase Technique. *IEEE Trans. Microw. Theory Tech.* **2025**, *73*, 8428–8440. https://doi.org/10.1109/TMTT.2025.3589813.
33. Zong, X.; Yang, F.; Xu, S.; Li, M. A Study of Spatial Quantization Effects on Reconfigurable Reflectarray Antennas. *IEEE Antennas Wirel. Propag. Lett.* **2025**, *24*, 2607–2611. https://doi.org/10.1109/LAWP.2025.3569917.
34. Farokhipour, E.; Chaychi Zadeh, M.A.; Zohrevand, S.; Rennings, A.; Nayyeri, V.; Komjani, N.; Erni, D. Anomalous Reflectors Using 2-Bit Coding Metasurfaces Under Oblique Incidence for Millimeter-Wave Applications. *IEEE Access* **2025**, *13*, 195904–195913. https://doi.org/10.1109/ACCESS.2025.3633558.
35. Shan, T.; Pan, X.; Li, M.; Xu, S.; Yang, F. Coding Programmable Metasurfaces Based on Deep Learning Techniques. *IEEE J. Emerg. Sel. Top. Circuits Syst.* **2020**, *10*, 114–125. https://doi.org/10.1109/JETCAS.2020.2972764.
36. Rossi, M.; Zhang, L.; Chen, X.Q.; Liu, C.; Castaldi, G.; Cui, T.J.; Galdi, V. Machine-Learning-Enabled Multi-Frequency Synthesis of Space-Time-Coding Digital Metasurfaces. *Adv. Funct. Mater.* **2024**, *34*, 2403577. https://doi.org/10.1002/adfm.202403577.
37. Bao, J.H.; Liu, C.; Zheng, Y.N.; Zhang, L.; Yu, W.M.; Li, L.; Cui, T.J. Physics-Informed Deep Learning Method for Real-Time Multi-Harmonic Beamforming Based on Space-Time-Coding Metasurface. *Adv. Electron. Mater.* **2026**, *12*, e00595. https://doi.org/10.1002/aelm.202500595.
38. Li, J.C.; Bao, J.H.; Liu, C.; Cui, T.J. Random Time-Space Coding Metasurfaces for Spatial Control of the Temporal Statistics of Electromagnetic Fields. *Adv. Sci.* **2026**, *13*, e21637. https://doi.org/10.1002/advs.202521637.
39. Zhan, H.; Gu, M.; Feng, H.; Tian, Y.; Zhu, M.; Zhou, H.; Jin, Y.; Tang, Y.; Wang, L.; Hong, Z.; et al. Dual-Channel Asymmetric Digital Transmission System Based on Weighted Theorem Optimized Coding Metasurface. *IEEE Trans. Commun.* **2026**, *74*, 8092–8102. https://doi.org/10.1109/TCOMM.2025.3635742.
40. Xie, T.; Lin, Y.L.; Li, A.; Qi, Z.J.; Wang, Z.X.; Xu, H.; Zhang, J.W.; Shao, R.W.; Luo, Z.J.; Dai, J.Y.; et al. A Global and Efficient Encoding Strategy for Beamforming Based on Branch-and-Bound Algorithm. *IEEE Trans. Antennas Propag.* **2026**, *74*, 2676–2685. https://doi.org/10.1109/TAP.2025.3650642.
41. Schuchman, L. Dither Signals and Their Effect on Quantization Noise. *IEEE Trans. Commun. Technol.* **1964**, *12*, 162–165. https://doi.org/10.1109/TCOM.1964.1088973.
42. Gray, R.M. Quantization Noise Spectra. *IEEE Trans. Inf. Theory* **1990**, *36*, 1220–1244. https://doi.org/10.1109/18.59924.

43. Gray, R.M.; Stockham, T.G. Dithered Quantizers. *IEEE Trans. Inf. Theory* **1993**, *39*, 805–812. https://doi.org/10.1109/18.256489.
44. Wannamaker, R.A.; Lipshitz, S.P.; Vanderkooy, J.; Wright, J.N. A Theory of Nonsubtractive Dither. *IEEE Trans. Signal Process.* **2000**, *48*, 499–516. https://doi.org/10.1109/78.823976.
45. Carbone, P.; Petri, D. Performance of Stochastic and Deterministic Dithered Quantizers. *IEEE Trans. Instrum. Meas.* **2000**, *49*, 337–340. https://doi.org/10.1109/19.843074.
46. Hadad, R.; Erez, U. Dithered Quantization via Orthogonal Transformations. *IEEE Trans. Signal Process.* **2016**, *64*, 5887–5900. https://doi.org/10.1109/TSP.2016.2599482.
47. Aysal, T.C.; Coates, M.J.; Rabbat, M.G. Distributed Average Consensus with Dithered Quantization. *IEEE Trans. Signal Process.* **2008**, *56*, 4905–4918. https://doi.org/10.1109/TSP.2008.927071.
48. Sun, Z.; Cui, W.; Liu, Y. Quantized Corrupted Sensing with Random Dithering. *IEEE Trans. Signal Process.* **2022**, *70*, 600–615. https://doi.org/10.1109/TSP.2022.3141884.
49. Yue, L.; Zhang, Y.; Wang, X.; Liu, H.; Chen, Z.; Li, J. The Importance of Dithering Technique Revisited with Biomedical Images—A Survey. *IEEE Access* **2019**, *7*, 3627–3634. https://doi.org/10.1109/ACCESS.2018.2888503.
50. Sheikh, S.; Kishk, A.A. Noise Shaping for Phased-Array Beamforming. *IEEE Trans. Antennas Propag.* **2022**, *70*, 6659–6670. https://doi.org/10.1109/TAP.2022.3161482.
51. Sheikh, S.; Kishk, A.A. Remarks on Noise Shaping for Phased Array Analog Beamforming. *IEEE Trans. Antennas Propag.* **2023**, *71*, 697–712. https://doi.org/10.1109/TAP.2022.3220936.
52. Jiang, H.; Jia, Y.; Wang, G.; Cai, Y.; Deng, H.; Gong, X. Globally Optimal Frequency-Partitioned Evolutionary Dithering for Binary Fourier Single-Pixel Imaging. *APL Photonics* **2025**, *10*, 086111. https://doi.org/10.1063/5.0276582.
53. Feuillen, T.; Vandendorpe, L.; Jacques, L. A Novel Multiplicative Phase Dithering Scheme for 1-Bit Compressive Radar. *IEEE J. Sel. Top. Signal Process.* **2025**, *19*, 1146–1158. https://doi.org/10.1109/jstsp.2025.3606387.
54. Kang, J.; Choi, J. Channel Estimation for One-Bit Quantized MIMO Systems: Dithering-Aided Approach. *IEEE Wirel. Commun. Lett.* **2026**, *15*, 2604–2608. https://doi.org/10.1109/LWC.2026.3682511.
55. Dassault Systèmes. *CST Studio Suite Student Edition*. Release 2024, Computer Software, 2024. Available online: https://www.3ds.com/edu/education/students/solutions/cst-le (accessed on 18 July 2026).
56. Ansys Inc. *Ansys HFSS—Student Version*. Computer Software. 2024. Available online: https://www.ansys.com/academic/students (accessed on 18 July 2026).

Disclaimer/Publisher's Note: The statements, opinions and data contained in all publications are solely those of the individual author(s) and contributor(s) and not of MDPI and/or the editor(s). MDPI and/or the editor(s) disclaim responsibility for any injury to people or property resulting from any ideas, methods, instructions or products referred to in the content.